International Journal of Nanomedicine

Dovepress
open access to scientific and medical research

Open Access Full Text Article

ORIGINAL RESEARCH

Combined miR-181a-5p and Ag Nanoparticles are Effective Against Oral Cancer in a Mouse Model

Guoqiang Xu[1,2,*], Xiaona Song[2,*], Xiaotang Wang[1,2,*], Rui Xue[1,2], Xiaoru Yan[1,2], Litao Qin[1,2], Xiaoqi Chang[1,2], Jiping Gao[1], Zhaoyang Chen[1], Guohua Song[1]

[1]Laboratory Animal Center Shanxi Key Laboratory of Experimental Animal Science and Human Disease Animal Model, Shanxi Medical University, Taiyuan, People's Republic of China; [2]School of Basic Medical Science, Shanxi Medical University, Taiyuan, People's Republic of China

*These authors contributed equally to this work

Correspondence: Guohua Song, Laboratory Animal Center, Shanxi Key Laboratory of Experimental Animal Science and Human Disease Animal Model, Shanxi Medical University, Road Xinjian 56, Taiyuan, 030001, People's Republic of China, Tel +86-351-4135919, Email ykdsgh@sxmu.edu.cn

Purpose: Oral squamous cell carcinoma is the most common type of malignant tumor in the head and neck region. Despite advancements, metastasis and recurrence rates remain high, and patient survival has not significantly improved. Although miRNA therapies are promising for cancer gene therapy, their applications in treating oral cancer are limited. Targeted medication delivery systems based on nanotechnology offer an efficient way to enhance oral cancer treatment efficacy.

Methods: We synthesized nanosilver (AgNPs) and loaded them with the tumor suppressor miR-181a-5p. In vitro experiments were conducted to investigate the inhibitory effects of AgNPs and their composites on the malignant behavior of oral cancer cell lines. The xenograft experiment was utilized to examine their effects on tumorigenesis and the potential molecular mechanisms involved.

Results: The nanosilver exhibited a spherical morphology with a size distribution ranging from 50 to 100 nm. They exhibited a distinct absorption peak at 330 nm and could be excited to emit green fluorescence. The biocompatible AgNPs effectively shielded miRNA from degradation by RNase and serum. The nanocomposites significantly inhibited the proliferation, invasion, migration, and colony formation of oral cancer cell lines. Notably, treatment with the nanocomposites resulted in substantial tumor growth suppression in the xenograft model. Mechanistically, these composites directly targeted BCL2 and exerted their antitumor effects by suppressing the β-catenin signaling pathway and other downstream genes without inducing acute toxicity.

Conclusion: Collectively, the findings demonstrate that the miR-181a-5p/AgNPs combination significantly impedes the growth and progression of oral cancer both in vitro and in vivo, highlighting a pivotal role for the β-catenin signaling pathway. This multifaceted approach holds promise as a prospective therapeutic strategy for oral cancer management in the future.

Keywords: silver nanoparticles, nanocomposite, combination therapy, β-catenin signaling pathway

Introduction

Squamous cell carcinoma makes up 90% of the malignant tumors in the oral and maxillofacial region.[1] Oral cancer frequently affects the lips, the hard palate, the floor of the mouth, the first two-thirds of the tongue, the upper and lower alveolar ridges, and the buccal mucosa.[2] The advancement of medical technology has led to significant progress in the treatment of oral cancer. However, the prognosis and treatment outcomes for patients with squamous cell carcinoma and mucosal precancerous lesions have not improved significantly due to the wide age range, complex lesions, and variety of patient types with oral cancer.[3] One of the main reasons is that conventional therapies like surgery, chemotherapy, and radiotherapy typically have significant side effects, and traditional clinical diagnosis often lags, delaying the optimal time to begin treatment.[4,5] Currently, oral cancer has a 5-year survival rate of about 55–60% following treatment. Researchers have increasingly focused on comprehensive treatment with several regimens to improve clinical efficacy because a single treatment modality has limited clinical success.

Received: 7 January 2024
Accepted: 20 June 2024
Published: 7 September 2024

Graphical Abstract

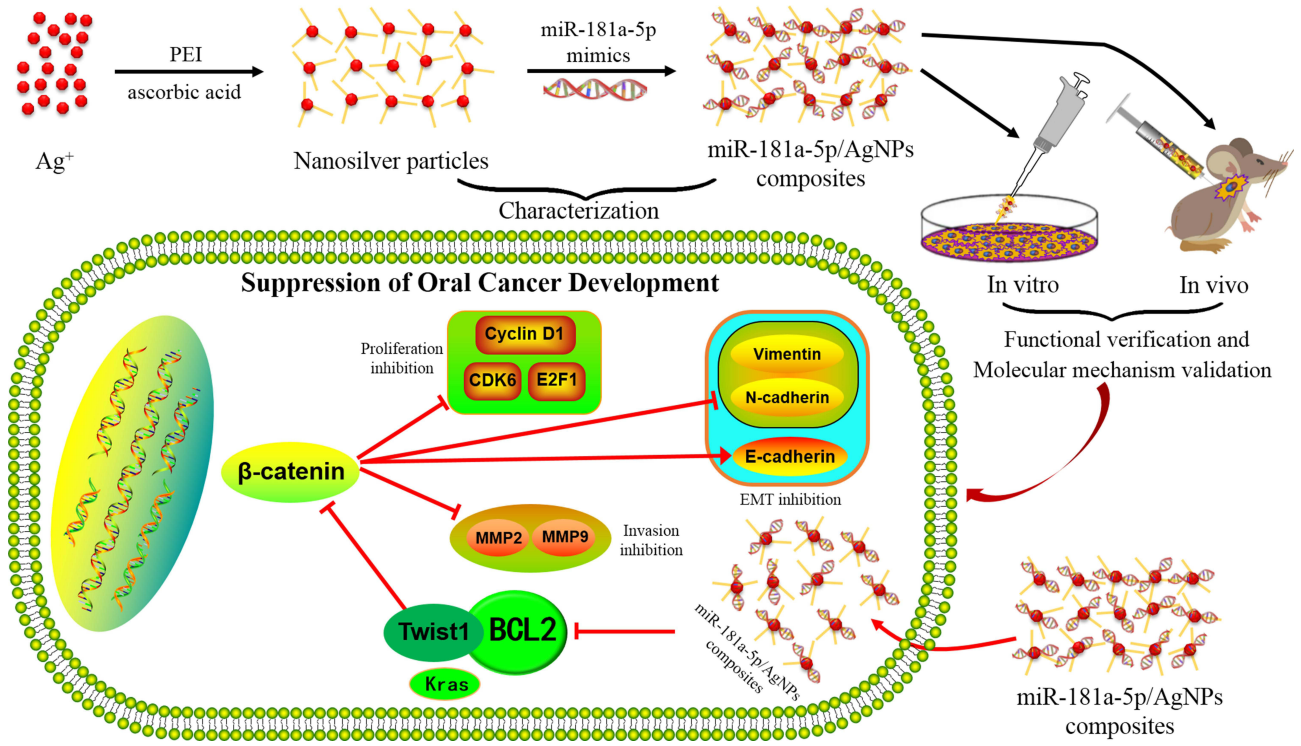

MicroRNAs (miRNAs) are endogenous short noncoding RNAs, approximately 22 nt in length, created by the stem-loop region of pri-miRNA.[6] Numerous studies indicate that miRNAs play a major role in the initiation and progression of cancer and are markedly differently expressed in oral cancer.[7–9] Based on our previous research findings, we observed that the expression of miR-181a-5p progressively decreases at each stage in the development of Chinese hamster buccal pouch mucosa, including normal mucosa, mucosal simple hyperplasia, mucosal dysplasia, and squamous cell carcinoma. Similarly, its expression is significantly downregulated in human oral cancer tissues and multiple human oral cancer cell lines. Moreover, miR-181a-5p exhibits potential tumor-suppressing activity against oral cancer. To better guide clinical applications, we conducted a search for its conservation and found that it is highly conserved among mammals.[10] These findings indicate that miR-181a-5p can be applied to the treatment of human oral cancer. Additionally, genes with high conservation often hold significant biological implications, thereby indirectly reflecting the importance of miR-181a-5p.

Park et al found that miR-181a-5p is significantly upregulated during replicative senescence in normal human oral keratinocytes. Since aging is also considered a tumor suppression mechanism, they investigated the expression and potential biological function of this gene in oral cancer. They discovered that it is frequently downregulated in oral cancer and can significantly inhibit proliferation and anchorage-independent growth ability. At the molecular level, they found that miR-181a-5p may act as an oral cancer suppressor by targeting Kras. Based on these findings, they propose that miR-181a-5p could be utilized for the treatment of oral cancer.[11] A study on chemoresistance in oral cancer found that the migration and invasion capabilities of cisplatin-induced drug-resistant oral cancer cell lines are significantly enhanced, accompanied by a marked downregulation of miR-181a-5p and upregulation of Twist1. Further functional validation demonstrated that miR-181a can reverse the chemoresistance of oral cancer cells and suppress their epithelial-mesenchymal transition (EMT) and metastasis by directly targeting Twist1.[12] A study on the metastasis of salivary adenoid cystic carcinoma (SACC) cells discovered that the upregulation of miR-181a-5p inhibited wound healing and invasion in SACC-LM cells.[13] Concurrently, research by He et al revealed that miR-

181a can suppress the migration, invasion, and proliferation of SACC cells in vitro, as well as tumor growth and lung metastasis in vivo, by directly targeting and inhibiting the expression of MAP2K1, MAPK1, and Snai2.[14] Jain et al found that miR-181a can inhibit the progression of SACC, making it a potential biomarker for diagnosis and prognosis.[15] A study on laryngeal squamous cell carcinoma (LSCC) indicated that miR-181a is downregulated in LSCC. Overexpression of miR-181a significantly inhibits proliferation, colony formation, invasion, migration, and EMT, while promoting apoptosis in LSCC cells.[16] Tang et al found that miR-181a-5p is downregulated in nasopharyngeal carcinoma (NPC) and can retard NPC development through negative regulation of KDM5C, suggesting its potential as a candidate therapeutic target for NPC treatment.[17] Recently, a study on biological aging revealed that miR-181a-5p can significantly induce cellular senescence and shorten cell lifespan, indirectly reflecting the potential tumor-suppressive function of miR-181a-5p.[18]

As miR-181a-5p has been recently discovered, there are only a few articles reporting its low expression in oral cancer; however, detailed investigations into its specific oral tumor-suppressive mechanisms and functional roles remain scarce. Additionally, unmodified miRNAs are highly susceptible to degradation and inactivation by certain substances within the complex internal environment of organisms, leading to their typically short half-life and necessitating frequent administration to maintain their effective concentration. In terms of drug absorption, after injection into the body, miRNAs must navigate through the circulatory system while evading uptake by the reticuloendothelial system and degradation by endogenous nucleases to reach their target organs. The size and negatively charged nature of miRNAs make it difficult for them to cross cell membranes and escape from endosomes on their own. To address the demands of miRNA-based illness treatment, it is imperative to design reliable, effective, and non-toxic targeted delivery systems.[19–21]

Ultrafine particulate materials, sometimes referred to as nanomaterials, exhibit unique qualities such as macroscopic quantum tunneling, surface effects, self-assembly, and quantum size effects.[22] Researchers have found that materials such as metals and metal oxide nanoparticles possess unique antitumor properties, making nanomaterials promising for a wide range of applications in tumor therapy. Among them, nanosilver, as an important member of the metallic nanomaterials family, has been confirmed to have good therapeutic effects and significant clinical application prospects.[23] It can inhibit proliferation and induce apoptosis by decreasing mitochondrial function, inducing the production of reactive oxygen species, releasing lactate dehydrogenase, causing cell cycle dysregulation, upregulating apoptosis-related genes, and inducing micronucleus formation, chromosomal aberrations, and DNA damage.[24,25]

Currently, many transfection reagents struggle to effectively escape from endosomes, resulting in excellent performance during in vitro cell transfection, but being cleared by cellular organelles such as lysosomes when used for in vivo therapy, thereby significantly reducing their therapeutic efficacy.[26] Nanosilver, however, is uniquely positioned to overcome this limitation. According to relevant literatures, compared to traditional transfection reagents, nanosilver offers the advantages of a smaller size, a high specific surface area, and the capability to easily penetrate biological membranes to enter cells.[24,25,27] This, in turn, aids the escape of nanosilver from intracellular endosomes. Moreover, silver possesses broad-spectrum antimicrobial[28] and multiple antitumor properties.[29,30] Therefore, utilizing nanosilver as a delivery carrier can significantly reduce the risk of contamination in the transfection system, offering a unique advantage and producing synergistic effects that are difficult to achieve with a single drug. Additionally, owing to the high permeability and retention effect of cancer cells, nanosilver can readily penetrate target cells and become selectively enriched within tumors. This makes nanosilver an effective drug delivery system.[31,32] In terms of economic feasibility, silver offers a lower cost option compared to precious metals, making it easier to synthesize and apply on a large scale. Silver also has stable properties, allowing for easy long-term storage and transportation after synthesis. Furthermore, numerous studies have reported that nanosilver can be utilized for early detection, diagnosis, and treatment of various types of cancer.[33–36] However, there is a notable scarcity of research specifically addressing the use of nanosilver in oral cancer. To further elucidate the possible therapeutic roles of significantly differentially expressed miR-181a-5p in oral cancer development and the specific inhibitory effects and mechanisms, further studies on nanosilver-conjugated miR-181a-5p are urgently needed.

In this study, the precision of gene therapy, the loading properties of nanomedicines, and their targeted delivery, high stability, and therapeutic properties were combined to explore their common effects on oral cancer treatment.

Material and Methods

The Synthesis of Nanosilver

Firstly, to ensure that the various raw materials did not absorb light on their own, we utilized a UV-VIS spectrophotometer to measure the absorbance of each raw material. We also explored the optimal conditions of pH, $AgNO_3$: PEI ratio, $AgNO_3$: AA ratio, and the stirring time (T) after adding the reducing agent AA. The detailed methods and results (Supplementary Figure 1) are attached to the Supplementary Methods 1 and Supplementary Results 1.

Briefly, ultrapure water, PEI 25K (Sigma, USA, 5 μmol/L), and $AgNO_3$ (Shanghai Sinopharm Chemical Reagent Co., Ltd., China, 0.1 mol/L) were slowly added to a beaker, which was sealed with plastic wrap. The pH of the system was adjusted to 4 using glacial acetic acid (Shanghai Aladdin Biochemical Technology Co., Ltd., China) after stirring for 2 h in the dark. Subsequently, ascorbic acid (AA) (Shanghai Aladdin Biochemical Technology Co., Ltd., China, 0.01 mol/L) was added. The total volume was adjusted to 20 mL using ultrapure water, and the solution was stirred at room temperature for 6 h under 365 nm UV light. The system was then transferred into an electric thermostatic blast drying oven at 45–55°C for 10–16 h. Finally, 20 mL of ultrapure water was added, and the mixture was ultrasonicated for 20–30 min to obtain a pure nanosilver solution. The charge of the synthesized nanosilver is positive.

The Characterization of Nanosilver

The AgNPs were characterized using a UV-8000 full-band UV-VIS spectrophotometer. Preliminary fluorescence characterization of AgNPs was performed under UV lamp irradiation. The fluorescent properties of AgNPs were further characterized using a chemiluminescent instrument (Syngene, UK). The optimal fluorescence excitation and emission wavelengths of AgNPs were scanned and detected using a fluorescence excitation and emission detector. The AgNPs solution was dropped onto a carbon-film copper grid, and the morphology of AgNPs was observed using a JEOL JEM-2100 transmission electron microscope (TEM) (JEOL Ltd., Tokyo, Japan). Nanoparticle size analyses were carried out by dynamic light scattering (DLS), and the AgNPs were also characterized by inductive coupled plasma (ICP).

Hemolysis Assay

To further evaluate the biocompatibility of AgNPs, we performed hemolysis experiments. Blood was obtained from the mouse orbit and immediately centrifuged at 3000 rpm for 5 min. The supernatant was removed, and the blood was washed with physiological saline to obtain red blood cells. Subsequently, 40 μL of red blood cells was added to 960 μL of physiological saline, deionized water, and samples of different concentrations (0.5, 1, 3, 5, and 10 mg/mL). Physiological saline and deionized water were used as negative and positive controls, respectively. All mixtures were incubated at 37°C for 1 h, then centrifuged at 5000 rpm for 5 min. After collecting images, 200 μL of supernatant was used to detect absorbance at a wavelength of 540 nm, and the hemolysis rate was calculated.

The Synthesis of Nanocomposites

The synthesis of nanocomposites begins by adding the AgNPs carrier to a centrifuge tube according to the specified proportion. miR-181a-5p mimics are then gradually added in the same proportion. The mixture is pipetted 40 to 50 times and incubated at room temperature for 20 to 30 min to synthesize the nanocomposite (miR-181a-5p/AgNPs).

Determination of the Optimal Loading Proportion of miR-181a-5p

The miR-181a-5p/AgNPs complexes synthesized at different molar ratios were loaded onto a 2% agarose gel for electrophoresis. The electrophoresis was performed at a constant voltage of 110 V for 15–20 min. After electrophoresis, the gel was developed using a chemiluminescent instrument (Syngene, UK) to determine the optimal ratio of miR-181a-5p mimics to nanosilver carriers.

The Characterization of Nanocomposites

Before testing, calibration was performed using ultrapure water (as the solvent) as the reference solution. The sample was diluted 15 times and added to a microplate for detection. The morphology of the nanocomposites was observed using a TEM. The size analyses of nanocomposites were further carried out by DLS.

The Detection of RNA Enzyme Stability of Nanocomposites

Both miR-181a-5p and miR-181a-5p/AgNPs were mixed with an equal volume of 0.05 mg/mL RNase solution and incubated in a CO_2 incubator for 1 h. After incubation, half of each solution was mixed with a 10 mg/mL heparin solution for 15 min. The samples were divided into four groups: miR-181a-5p + RNase, miR-181a-5p + RNase + heparin, miR-181a-5p/AgNPs + RNase, and miR-181a-5p/AgNPs + RNase + heparin. The solutions from each group were electrophoresed on a 2% agarose gel for 15–20 min at 110 V.

The Detection of the Serum Stability of Nanocomposites

Both miR-181a-5p and miR-181a-5p/AgNPs solutions were mixed with an equal volume of serum and incubated in a CO_2 incubator for 2, 4, 6, 8, 10, 12, and 24 h, respectively. After incubation, half of each sample was mixed with a 2% SDS solution for 15 min. The samples were divided into four groups: miR-181a-5p + FBS, miR-181a-5p + FBS + 2% SDS, miR-181a-5p/AgNPs + FBS, and miR-181a-5p/AgNPs + FBS + 2% SDS. After all groups were incubated, they were electrophoresed for 15–20 min at 110 V on a 2% agarose gel.

Cell Culture

The human oral cancer cell lines CAL-27, SCC-9, the Chinese hamster ovary cell line CHO, and human neural cells SH-SY5Y and HT22 were purchased from Procell Life Science & Technology Co., Ltd. (Hubei, China). The 293T, HN6, and SCC-25 cell lines were provided by Henan Provincial People's Hospital. CAL-27, CHO, SCC-9, HN6, and 293T, and HT22 cells were cultured in Dulbecco's modified Eagle's medium (DMEM). SCC-25 and SH-SY5Y cells were grown in DMEM/F12 medium. The medium contained 10% fetal bovine serum (Gibco, USA) and 1% penicillin and streptomycin solution (Solarbio, China). The cells were maintained at 37°C in a CO_2 incubator.

Quantitative Real-Time PCR

Total RNA from tissues and cell lines was isolated using TRIzol (Takara, Japan). Reverse transcription of miRNA was performed using the Mir-X miRNA First Strand Synthesis Kit (Takara, Japan), and cDNA of mRNA was synthesized using the PrimeScript RT Master Mix Kit (Takara, Japan). Quantitative real-time PCR (qPCR) was performed using the SYBR Green PCR Master Mix Kit (Takara, Japan) on a StepOne Plus system (ABI, USA). The primers synthesized by Beijing Genomics Institute (BGI, China) are listed in Table 1. The quantification of miRNA and mRNA was performed according to the manufacturer's instructions, with U6 and β-actin used as internal references. The $2^{-\Delta\Delta CT}$ method was used to analyze the results.

Transfection Efficiency Detection of Nanocomposites in Multiple Cell Lines

Unrelated sequences were used as negative controls (NC group). One hour before transfection, the medium was replaced with fresh medium. In tube A, the nanosilver carrier was added, followed by 250 μL/well of medium, gently pipetted to mix, and incubated at room temperature for 5 min. miR-181a-5p mimics or NC were added to tube B, followed by 250 μL/well of medium. The B solution was then added to the A solution, mixed thoroughly, and incubated at room temperature for 30 min. The mixture was added to the corresponding wells and replenished to 2 mL with medium. The culture continued, with the medium replaced with complete medium 6 h after transfection. Twenty-four hours post-transfection, the medium in each well was aspirated, and the wells were gently washed twice with PBS. TRIzol was added to lyse the cells and extract RNA from each group. The expression of miR-181a-5p was quantified after reverse transcription. miR-181a-5p mimics (5'-AACAUUCAACGCUGUCGGUGAGU-3', 5'-UCACCGACAGCGUUGAAUGUUUU-3') and its corresponding negative control (miR-181a-5p mimics NC: 5'-UUCUCCGAACGUGUCACGUTT-3', 5'-ACGUGACACGUUCGGAGAATT-3') were purchased from GenePharma Inc. (Shanghai, China).

Table 1 Primer Sequence Information

Name	Sequence (5'-3')
β-actin	F: CATGTACGTTGCTATCCAGGC
	R: CTCCTTAATGTCACGCACGAT
BCL2	F: TTTGTGGAACTGTACGGCCC
	R: TCACTTGTGGCCCAGATAGG
Kras	F: TGTGGACGAATATGATCCAACA
	R: GCAAATACACAAAGAAAGCCCT
Twist1	F: TGTCCGCGTCCCACTAGC
	R: TGTCCATTTTCTCCTTCTCTGGA
Cyclin D1	F: ATGTTCGAGGCGCGCCTGGTC
	R: CTAAGATCCTTCTTCATCCTC
CDK6	F: GTGACCAGCAGCGGACAAATAA
	R: AGCAAGACTTCGGGTGCTCTGTA
MMP9	F: ACGCACGACGTCTTCCAGTAC
	R: ACCTGGTTCAACTCACTCCGG
MMP2	F: TTGACGGTAAGGACGGACTC
	R: GGCGTTCCCATACTTCACAC
E2F1	F: AGCTGGACCACCTGATGAATATCTG
	R: TTGATCACCATAACCATCTGCTCTG
Vimentin	F: GAAGAGAACTTTGCCGTTGA
	R: CGAAGGTGACGAGCCATT
U6	CGCTTCGGCAGCACATATAC
miR-181a-5p	CATTCAACGCTGTCGGTGAGTA

Effect of Nanocomposites Transfection on Target Genes and Selection of Target Cell Lines

Similarly, transfections were performed after seeding cells in six-well plates (at 2×10^5 cells/well), and RNA from each group was isolated using TRIzol. Reverse transcription and quantification of target genes were performed following the procedure described above. Primer sequence information for the target genes is shown in Table 1.

Research on the Uptake of Nanosilver by Oral Cancer Cell Lines

Cells to be transfected were seeded in dishes 24 h before transfection. The nanosilver solution was added to each group and replenished to 2 mL with medium. Six hours post-transfection, the medium was replaced with complete medium. Twenty-four to forty-eight hours after transfection, the medium from each dish was aspirated, and the wells were gently washed twice with PBS. The laser confocal microscope was adjusted to the optimal excitation wavelength of AgNPs and subsequently used for microscopic examination and photography.

Determination of Nanosilver Transfection Efficiency of miR-181a-5p

To detect the transfection efficiency of nanosilver, miR-181a-5p was labeled with FAM. The transfection procedure was performed as previously described. The laser confocal microscope excitation wavelength was adjusted to the optimal excitation wavelength of the FAM label, and each dish was then examined and photographed.

CCK8 Assay

Cells were seeded into 96-well plates (5×10^3 cells/well). Transfection was performed after the 96-well plates were incubated overnight. At 0, 24, 48, and 72 h, the CCK8 reagent was added to each well. After 2 h of incubation at 37°C, the absorbance was detected at 450 nm.

Colony Formation Assay

Cells were seeded into six-well plates and incubated overnight. Forty-eight hours post-transfection, cells were collected and counted. Each group was subsequently seeded into six-well plates at a density of 2000–5000 cells per well. After approximately 15 days, the cells were washed twice with PBS. The cells were then fixed with paraformaldehyde for 30 min, stained with 0.1% crystal violet for 30 min, and washed three times with PBS. The cells in each group were photographed and counted.

Cell Invasion Assay

The cell invasion assay was performed using Transwell chambers (Corning, USA). The necessary materials were pre-cooled, including Matrigel, pipette tips, and centrifuge tubes, at 4°C. The transwell chamber was covered with 100 μL of Matrigel™ (Corning, USA) and dried in an incubator. Cells from each group (5×10^3) were resuspended in 100 μL of serum-free medium after 48 h of transfection and seeded in the upper chamber. Complete medium was added to the lower chamber and the plate was transferred to an incubator for 24 h. The medium was aspirated from the upper chamber, each chamber was washed twice with PBS, and the upper chamber was gently scratched with a cotton swab. The cells were fixed with 4% paraformaldehyde for 30 min, stained with 0.1% crystal violet for 20 min, washed with PBS three times, and photographed and counted under a light microscope.

Cell Migration Assay

The cell migration assay followed the same steps as the cell invasion assay, except the upper chamber was not treated with Matrigel.

Detection of Cell Morphology and Pathological Changes

A little PBS was added to each well of a six-well plate and a 75% alcohol-treated coverslip was placed on the PBS in each well. Log-phase cells were collected and counted, then 3.0×10^4 cells were plated on each coverslip. After 48 h, the cells were washed twice with PBS and fixed with 4% paraformaldehyde for 30 min. HE staining was performed following the manufacturer's instructions and the slides were analyzed under a light microscope.

Oxidative Stress Detection

After seeding an appropriate amount of neural cells into a 6-well plate, transfer the plate to the incubator for overnight culture. And perform transfection according to the preceding steps. Subsequently, the levels of ROS, MDA, SOD, CAT, LDH, and GSH in the two types of neuronal cells were assessed using the appropriate detection kits (Nanjing JianCheng, Nanjing, China) and their corresponding assay procedures.

Screening the Target Gene of miR-181a-5p

The target genes of miR-181a-5p were predicted using miRTarBase[37] and visualized with Cytoscape. Targetscan (http://www.targetscan.org) was used to predict the binding sites of miR-181a-5p and its target gene.

Dual-Luciferase Reporter System to Validate the Target Gene

Wild- and mutant-type plasmids of the target gene were constructed. A 24-well plate was seeded with 1×10^5 293T cells per well. When the cells reached 80% confluence, Lipo 3000 transfection reagent was used to co-transfect the constructed reporter plasmids with miR-181a-5p sequence or miR-181a-5p negative control. After 48 h, the medium was removed, cells were washed twice with PBS, and the detection steps according to the kit protocol were followed (TransGen Biotech, China). Supplementary Materials included the sequences of wild-type and mutant BCL2 mRNA 3'UTR (Supplementary Table 1) and detailed information about the plasmids (Supplementary Figure 2).

Verification of Downstream Gene Expression

Total RNA was extracted from tissues and transfected cells, reverse transcribed, and quantified by qPCR, following the procedures described earlier. Relevant primers for the detected genes are listed in Table 1.

Detection of Downstream Proteins

Total protein was extracted from tissues and transfected cells, 15 μg/well of each protein was loaded on 10% SDS-PAGE, and the separated protein samples were transferred to polyvinylidene fluoride membranes. After blocking at room temperature, the membranes were incubated with the following antibodies overnight at 4°C: anti-BCL2 (1:800 dilution; Abcam, USA), anti-Kras (1:1000 dilution; Proteintech, China), anti-Twist1 (1:600 dilution; Proteintech, China), anti-MMP9 (1:1000 dilution; abclonal, China), anti-MMP2 (1:1000 dilution; Proteintech, China), anti-E-cadherin (1:1000 dilution; abclonal, China), anti-N-cadherin (1:1000 dilution; Proteintech, China), anti-Vimentin (1:1000 dilution; Proteintech, China), anti-β-catenin (1:1000 dilution; BOSTER, China), and anti-β-actin (1:5000 dilution; BIOSS, China). Next, they were incubated with a conjugated secondary antibody (TransGen Biotech; 1:5000) for 1 h at room temperature. The protein bands were detected and photographed using an enhanced chemiluminescence detection system. The grayscale was analyzed using ImageJ software, with β-actin as the internal control.

Construction of a Tumor Xenograft Animal Model

Fifteen 4-week-old female nude mice (18–22 g) were purchased from Gempharmatech Biotechnology Co., Ltd. (Jiangsu, China) and raised in the Experimental Animal Center of Shanxi Medical University (Taiyuan, China). All experimental procedures were strictly performed according to the Guidelines for Ethical Review of Laboratory Animal Welfare in China (GB/T3589-2018). All experimental procedures were approved by the Animal Care and Use Committee of Shanxi Medical University (SYDL2023015). The oral cancer cell line CAL-27 (5×10^6/mice) was subcutaneously injected into the left armpit. The tumor volume was calculated using the formula: length × Width^2 × 1/2.

In Vivo Therapy

After successful establishment of the xenotransplantation model, 15 nude mice were randomly divided into the control group (PBS), carrier group (negative control group, AgNPs/NC), and treatment group (AgNPs/miR-181a-5p) when their tumors grew to about 100 mm^3. Five animals in each group were intraperitoneally injected twice a week (15 mg/kg) for treatment. The tumor volume was measured with a vernier caliper every 2 days.

Analysis of Tumor Inhibition

After 21 days of treatment, the mice were euthanized, and the tumors were collected and weighed. The tumor inhibition rate was calculated as follows: (1 − tumor weight of treated group / tumor weight of control group) × 100%. Tumor growth inhibition was calculated as follows: [1 – (average tumor volume on the last day in the treated group – average tumor volume before treatment in the treated group) / (average tumor volume after treatment in the control group – average tumor volume before treatment in the control group)].

Body Weight Monitoring and Detection of Body Weight Inhibition Rate

The activity, diet, and mental state of animal models were observed every day. Body weight was monitored every 2 days. The body weight inhibition rate was calculated as follows: (1 – body weight of the mice after treatment / body weight of the mice before treatment) × 100%.

Pathological and Organ Coefficient Analysis

After 21 days of treatment, the mice were euthanized, and the tumor, heart, liver, spleen, lung, kidney, and other major organs of each group were collected for further molecular and pathological analysis. The organ coefficients (the ratio of organ weight to body weight) of each major organ were calculated. H&E pathological staining was performed using the corresponding kits from BOSTER Biological Technology Co., Ltd. (Wuhan, China) according to the attached protocol.

Immunohistochemical Verification of Molecular Mechanisms In Vivo

Target and downstream protein expression in oral cancer tissues were detected using the SABC kit (Boster, China). Slicing and dehydration were consistent with the HE examination. Endogenous peroxidase activity was blocked with 3% H_2O_2. Heat-induced epitope retrieval was performed using a citrate buffer. The slices were then incubated with the primary antibody (diluted 1:100) overnight at 4°C, followed by incubation with the secondary antibody (diluted 1:800) for 30 min at 37°C. Kit protocols were followed for the remaining steps. Finally, the sections were examined under a light microscope, and cells with brown cytoplasm or membrane were identified as positive.

Statistical Analysis

All data are presented as mean ± standard deviation. Student's *t*-test was used for statistical comparisons. *P < 0.05 was considered significant, and **P < 0.01 was considered highly significant.

Results

Evaluation of the Physical Properties of Nanosilver

As shown in Figure 1A, AgNPs exhibited higher absorbance values and smoother absorbance curves. The curves did not have obvious multipeaks and peak shoulders and were uniform and narrow, with one maximum absorption peak at 330 nm. AgNPs emitted green fluorescence when exposed to UV light, whereas the other raw materials used in the synthesis only illuminated under UV light without visible fluorescence (Figure 1B and C). The fluorescence of the AgNPs solution in a small beaker showed obvious yellow-green fluorescence under UV light (Figure 1D). As depicted in Figure 1E and F, AgNPs exhibited distinct outlines under UV excitation, while other components showed no discernible images. This observation further substantiates that AgNPs can indeed emit fluorescence under UV light excitation.

We found that the optimal excitation wavelength of AgNPs is 437 nm, at which point the fluorescence intensity was 1390. The optimal emission wavelength was 524 nm, with a fluorescence intensity of 1394 (Figure 1G). Transmission electron microscopy revealed that the AgNPs had a spherical structure with a small globular shape, uniform in size and dispersion (Figure 1H). The size of AgNPs mostly ranged from 40–80 nm, as observed by transmission electron microscopy (TEM). The results of ICP (Table 2) confirmed that AgNPs contained a certain amount of Ag element, illustrating that the AgNPs were indeed silver-containing particles from an elemental, qualitative, and quantitative perspective. Nanoparticle size analysis (Figure 1I) showed that the AgNPs were well dispersed with a uniform size, most of them around 40 nm.

Evaluation of the Biosafety of Nanosilver

Good biocompatibility is crucial for constructing a nanoco-delivery system. We performed a hemolysis assay to evaluate the biocompatibility of AgNPs. The results showed that AgNPs have good biocompatibility, with hemolysis rates at various concentrations significantly lower than 5% (Figure 1J and K). Even at a concentration of 10 mg/mL, the hemolysis rate was only 2.16%, indicating that AgNPs could be used for subsequent experiments.

The Optimal Ratio for Loading miR-181a-5p

The amount of miR-181a-5p remaining in solution decreased with increasing AgNPs usage, as shown by the results of loading miR-181a-5p mimics sequence by AgNPs (Figure 2A). Therefore, the amount of sequence able to run out of the gel is also gradually reduced, corresponding to the lower brightness in the lane. The miRNA well is the brightest because no miRNA is loaded on the carrier, so all miRNAs in the well run down with electrophoresis, making the band corresponding to this well the lightest. No band brightness was exhibited in the loading well for miRNAs not tethered by the carrier. The AgNPs group, having no nucleic acid, showed no bands in the lanes and no brightness in the loading well.

At the 0.125:1 ratio, only a small portion of miRNAs could be tethered to the loading wells without running into the corresponding lanes due to the low content of nanocarriers, resulting in darker brightness in the loading wells and more distinct bands in the corresponding position in the lane. At a 0.5:1 ratio, the majority of miRNAs were loaded onto the carrier, with only a small fraction of unentrapped miRNAs reaching the corresponding position in the lane. At a 1:1 ratio, all miRNAs were

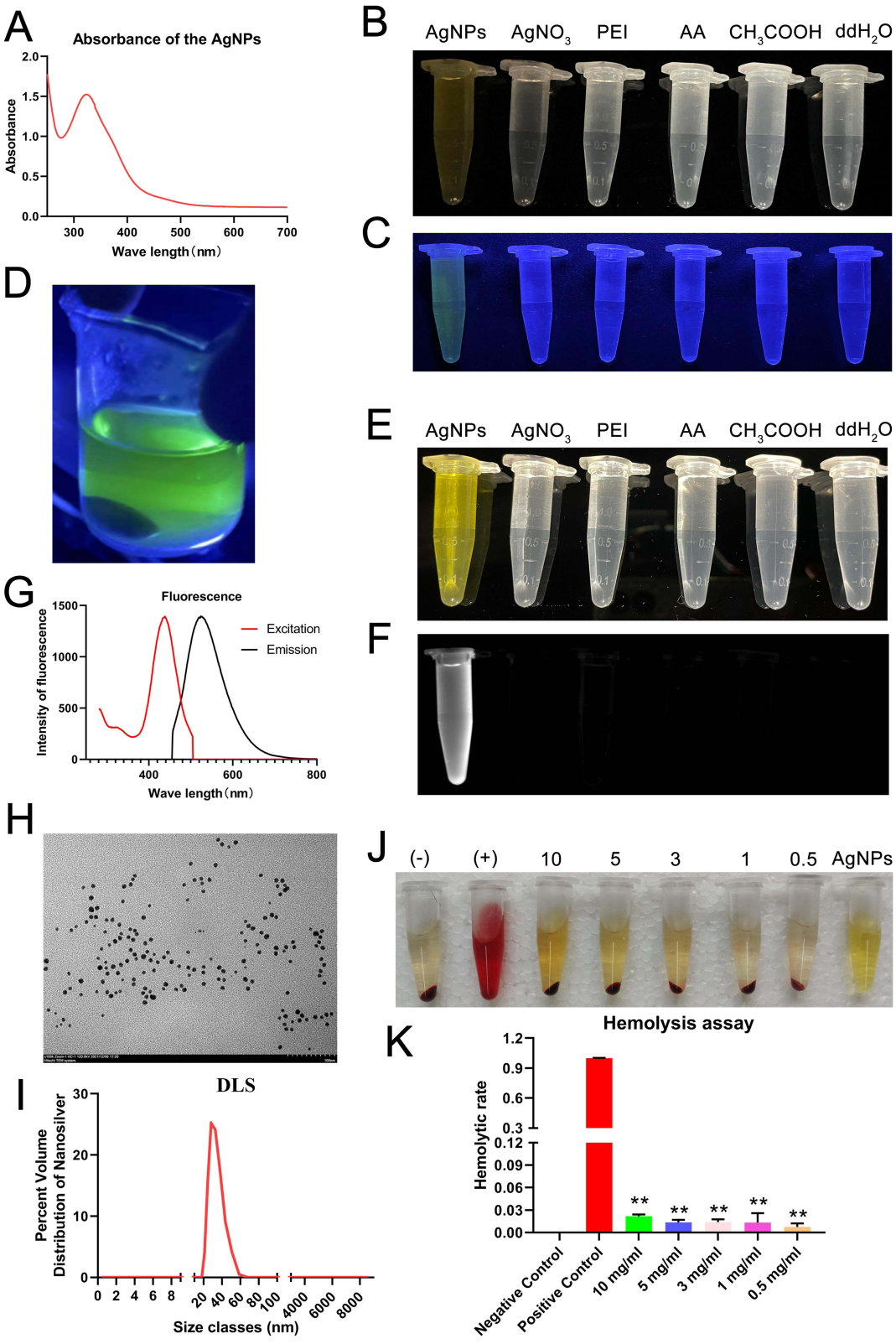

Figure 1 Synthesis and characterization of AgNPs. (**A**) UV-Vis characterization of AgNPs. (**B**). Normal light images; (**C**). Ultraviolet radiation exposed images of AgNPs. (**D**) Ultraviolet irradiated AgNPs in a small beaker post-synthesis. (**E**). Normal light view of AgNPs in the chemiluminescent instrument. (**F**) Image of AgNPs in the exposure mode of the chemiluminescent instrument. (**G**) Determination of optimal excitation and emission wavelengths for AgNPs. (**H**) Characterization of AgNPs by transmission electron microscopy. (**I**) Particle Size Analysis of AgNPs. (**J**) Digital photographs of each group. (**K**) Hemolysis rate analysis for AgNPs at different concentrations.
Notes: **compared with the positive control group, $P < 0.01$.

Table 2 Identification of AgNPs by ICP

Sample	Volume/mL	Dilution Coefficient	Readings	Content
Repeat 1	1	1	0.9766	24.4145
Repeat 2	1	1	0.9206	23.0146
Average	1	1	0.9486	23.7146

tethered in the loading well by the carrier. Similarly, in the 2:1 and 3:1 groups, all miRNAs were fully loaded on the nanocarrier, tethered to loading wells, and did not electrophorese into lanes. Therefore, we chose the molar ratio of the nanosilver carrier to miR-181a-5p at 1:1 as the final ratio to prepare the composite drug loading system of nanosilver.

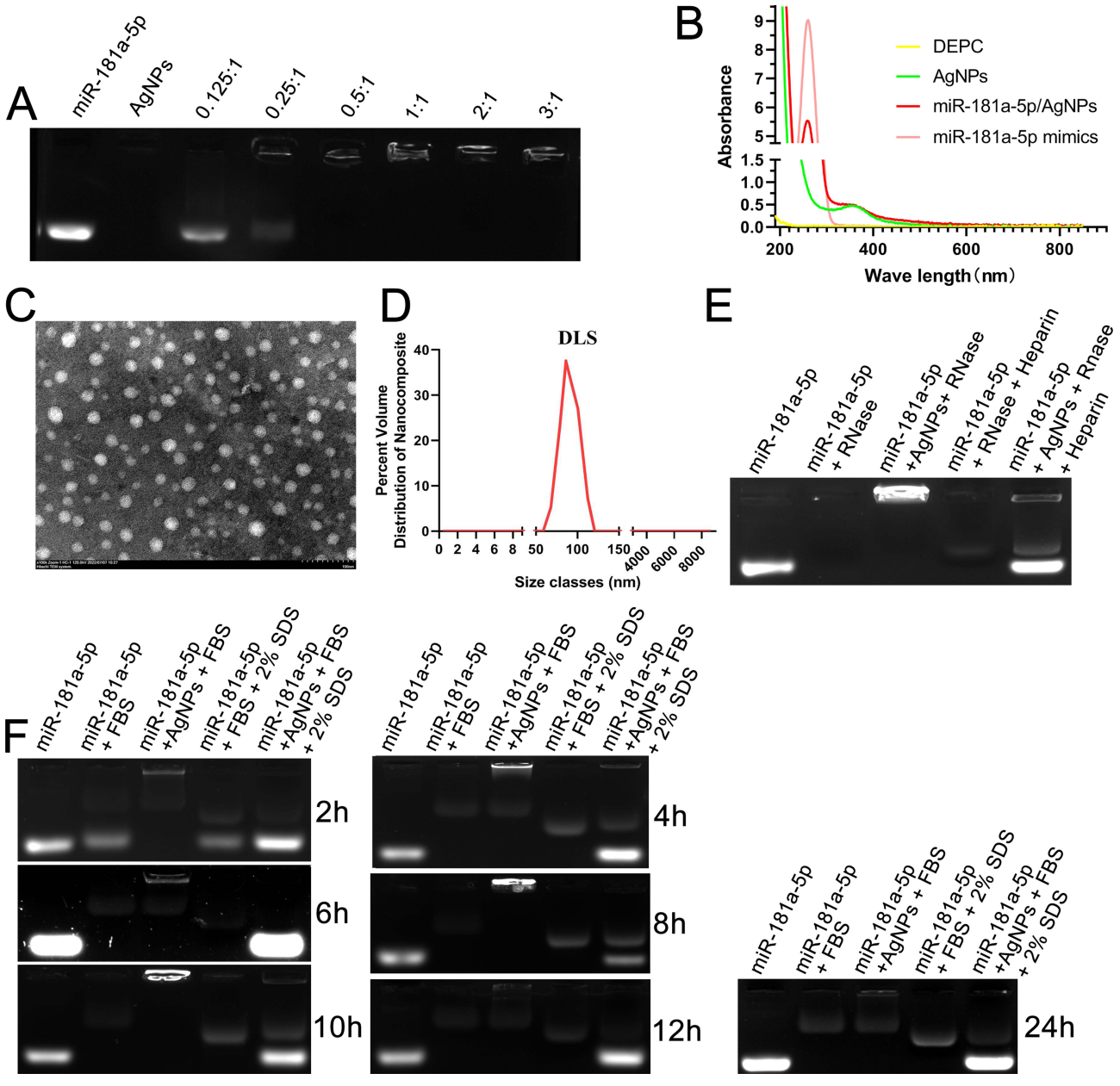

Figure 2 Synthesis and characterization of nanocomposite. (**A**) Research on the optimal proportion of AgNPs loading miR-181a-5p. (**B**) UV-Vis characterization of nanocomposite. (**C**) Characterization of nanocomposite by transmission electron microscopy. (**D**) Characterization of particle size of nanocomposite. (**E**) RNase stability characterization of nanocomposite. (**F**) FBS stability characterization of nanocomposite.

Characterization of the Nanocomposite

As shown in Figure 2B, the miR-181a-5p/AgNPs composite has characteristic absorption peaks not only at the characteristic peak position of AgNPs but also at OD 260 nm, the characteristic absorption peak of nucleic acid. This result indicates that the composite contains both nanosilver clusters and nucleic acids, confirming that miR-181a-5p was successfully loaded onto the AgNPs. TEM characterization (Figure 2C) revealed that the composite exhibited a spherical structure with particle sizes mostly distributed in the range of 80–120 nm. DLS examination of the composite also showed particle sizes mainly in the range of 80–120 nm (Figure 2D). TEM and DLS characterizations revealed no significant alteration in the morphology of the nanocomposites after loading with miR-181a-5p.

RNase Stability Assay of Nanocomposite

RNases can degrade RNA fragments quickly, but miRNAs are protected from degradation by RNases when loaded onto nanocarriers. Heparin and SDS can affect the binding of miRNA to nanocarriers, so when miR-181a-5p/AgNPs and heparin (or SDS) are co-incubated, the miR-181a-5p is released and shows a clear band.

To demonstrate that AgNPs protect the loaded miRNAs, we assessed the RNase stability of the miR-181a-5p/AgNPs composites (Figure 2E). In the miR-181a-5p group, miR-181a-5p did not co-incubate with RNase, so it consistently moved with electrophoresis, showing a clear, bright band. When miR-181a-5p and RNase were incubated together for 1 h, miR-181a-5p was degraded by RNase, resulting in no clear band in the miR-181a-5p + RNase group. In the miR-181a-5p/AgNPs + RNase group, miR-181a-5p was protected by the carrier and thus neither ran toward the positive electrode nor was degraded by RNase, resulting in a bright band in the loading well. In the miR-181a-5p + RNase + heparin group, miR-181a-5p was degraded during the previous incubation, producing no distinct bands. In the miR-181a-5p/AgNPs + RNase + heparin group, miR-181a-5p was protected from degradation by the AgNPs carrier during RNase incubation. Heparin affected the binding of miRNA to nanocarriers, causing miR-181a-5p to detach from the composites and shift down during electrophoresis, resulting in bright bands at the same position as the miR-181a-5p group. In summary, the AgNPs carrier has a strong protective effect on miR-181a-5p and can effectively protect it from RNase degradation.

Serum Stability Assay of Nanocomposite

To confirm that AgNPs protect the targeted miRNA and to better simulate the microenvironment of nanocarriers and nucleic acid sequences in transfected cells and within the body, we characterized the serum stability of miR-181a-5p/AgNPs composites. The results (Figure 2F) showed that the AgNPs carrier well-protected miR-181a-5p, ensuring its stability in serum for a longer period. The single miR-181a-5p sequence was almost completely degraded when incubated in 50% serum for 4–6 h. However, the miR-181a-5p sequence in the miR-181a-5p/AgNPs composite was released smoothly after incubation in 50% serum for up to 24 h, showing a bright band at the corresponding position. Therefore, the AgNPs carrier can protect the miR-181a-5p sequence in serum.

Detection of the Transfection Efficiency of Nanocomposite

The transfection efficiency verification experiment showed that AgNPs can successfully carry the target miR-181a-5p mimic sequence into the cell and release it smoothly (Figure 3A). The results indicate that the AgNPs carrier has high transfection efficiency in various cell lines, laying the foundation for subsequent mechanism validation experiments.

When verifying the transfection efficiency of AgNPs, we found that when the molar ratio of the carrier to the sequence was 1:1, the expression of the target sequence maintained a high level. Therefore, we chose a 1:1 loading ratio for subsequent experiments.

Effects of Nanocomposite on Downstream Genes and Screening of Target Cell Lines

The changes in downstream genes in each cell line are shown in Figure 3B. According to the results, in SCC-25 and CAL-27 cell lines, the miR-181a-5p/AgNPs composite exhibits the most significant inhibitory effect on downstream target genes. Therefore, we selected SCC-25 and CAL-27 for subsequent functional verification experiments.

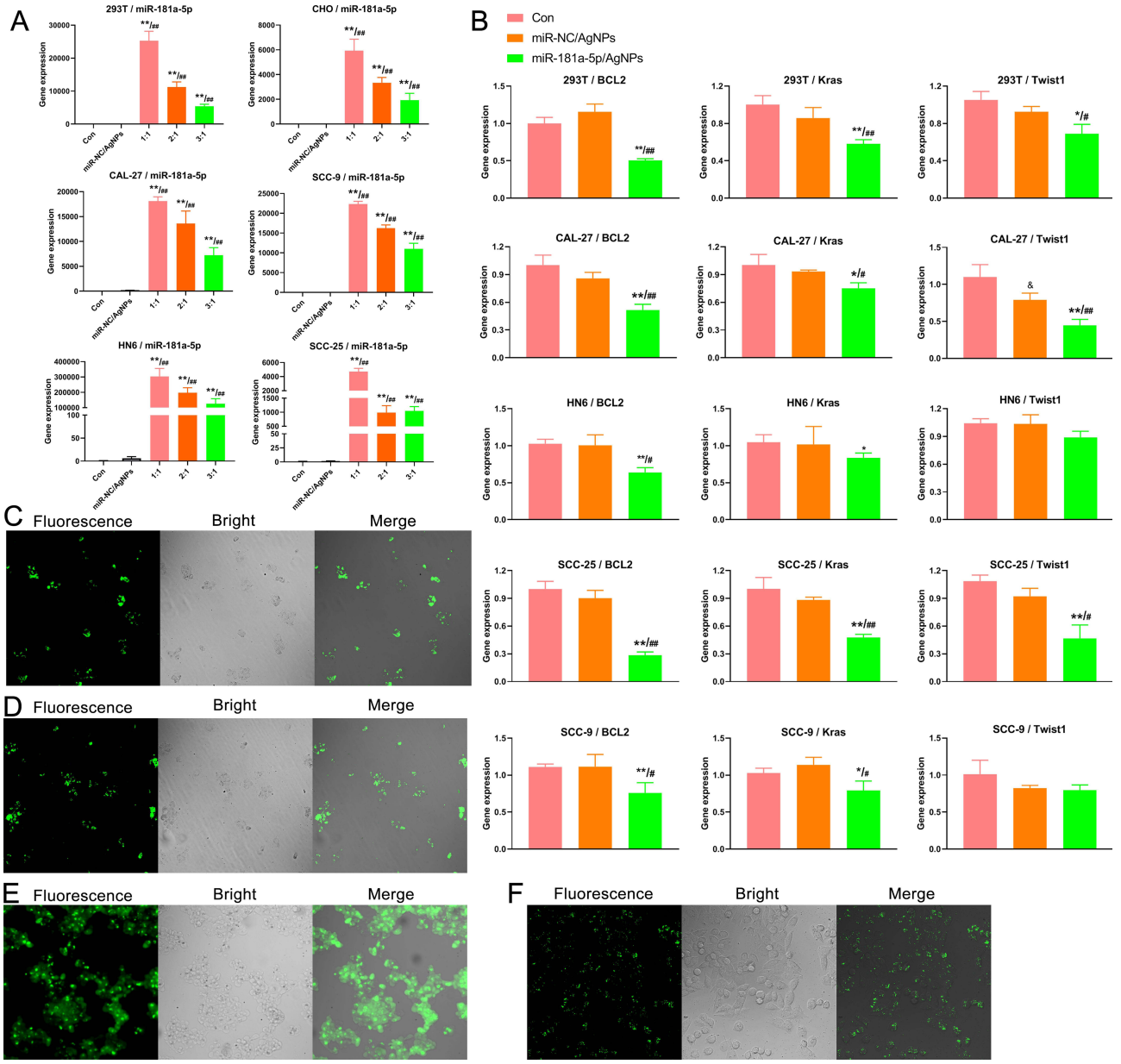

Figure 3 Screening of target cell lines and identification of transfection efficiency. (**A**) Transfection efficiency detection of AgNPs in distinct cell lines. On the x-axis, the ratios 1:1, 2:1, and 3:1 represent different molar proportions of carrier AgNPs to miR-181a-5p sequence. (**B**) Expression levels of three downstream genes across various cell lines. (**C**) and (**D**). Detection of fluorescence in AgNPs following transfection in SCC-25 (**C**) and CAL-27 (**D**) cell lines. (**E**) and (**F**). Assessment of transfection efficiency of AgNPs in SCC-25 (**E**) and CAL-27 (**F**) cell lines using FAM-tagged miR-181a-5p.

Notes: *: miR-181a-5p/AgNPs group compared with the Con group, $P < 0.05$; **: miR-181a-5p/AgNPs group compared with the Con group, $P < 0.01$; #: miR-181a-5p/AgNPs group compared with the miR-NC/AgNPs group, $P < 0.05$; ##: miR-181a-5p/AgNPs group compared with the miR-NC/AgNPs group, $P < 0.01$; and: miR-NC/AgNPs group compared with the Con group, $P < 0.05$.

The Uptake of Nanosilver by Oral Cancer Cell Lines

After transfecting the two cell lines with AgNPs, it was shown that AgNPs could enter the two cell lines smoothly, demonstrating high transfection efficiency and producing obvious green fluorescence in the cells (Figure 3C and D). From the results, it is evident that AgNPs have good transfection ability and can be used as a new carrier to transport drugs into cells. Additionally, AgNPs exhibit favorable fluorescence properties, emitting green fluorescence upon excitation and displaying clear images within oral cells. This suggests that AgNPs may hold potential for use as drug tracers.

Determining the Transfection Efficiency of Nanosilver

AgNPs were used as a carrier to transport miR-181a-5p mimics with a FAM tag to transfect the two cell lines. The results showed that AgNPs could not only enter the cells but also carry nucleic acid sequences into the cells smoothly, indicating that AgNPs can serve as a new type of nucleic acid transfection carrier. The transfection results indicated that most cells contained varying degrees of green fluorescence (Figure 3E and F), confirming that AgNPs have high transfection efficiency.

Nanocomposite Inhibits the Proliferation of Oral Cancer Cell Lines

Compared with the control group and the AgNPs/NC group, the miR-181a-5p/AgNPs composite significantly inhibits the proliferation of oral cancer cell lines (Figure 4A and B). Notably, AgNPs alone also exhibit an inhibitory effect, with the proliferation rate of the AgNPs group being significantly lower than that of the control group.

Nanocomposite Inhibits the Colony Formation of Oral Cancer Cell Lines

A colony formation experiment was conducted to determine the effect of miR-181a-5p/AgNPs on the growth and development of human oral cancer cell lines. The results showed that AgNPs and their composites significantly inhibit the formation of oral cancer cell colonies. Compared with the blank group and the AgNPs/NC group, the miR-181a-5p/AgNPs complex has a more significant inhibitory effect on the colony formation of oral cancer. The inhibitory effect of the miR-181a-5p/AgNPs complex is significantly stronger than that of the AgNPs/NC group (Figure 4C–H).

Nanocomposite Inhibits the Invasion of Oral Cancer Cell Lines

The invasion results (Figure 5A–D) show that miR-181a-5p/AgNPs significantly reduces the invasive ability of oral cancer cells compared with the control and AgNPs/NC groups. Additionally, AgNPs alone can inhibit the invasion of oral cancer cells to a certain extent.

Nanocomposite Inhibits the Migration of Oral Cancer Cell Lines

The migration results show that miR-181a-5p/AgNPs composites significantly inhibit the migration of oral cancer cells (Figure 5E–H). While the AgNPs carrier itself also inhibits migration, its effect is significantly lower than that of the miR-181a-5p/AgNPs group.

Cell Morphology and Pathological Changes

To assess the impact of AgNPs and miR-181a-5p/AgNPs on the pathological morphology of oral cancer cell lines, HE staining was employed to observe cellular morphological alterations. The results showed that the cells in the control group were short and spindle-shaped, tightly adherent, with clear and large nuclei, and structurally intact cell membranes (Figure 5I and J). Some cells in the AgNPs group maintained their original short spindle type, while others had loose adherence and exhibited ellipsoid shapes (Figure 5I and J). Meanwhile, the cells in the composite group typically tended to have a round shape with swelling and disintegration of some nuclei, exhibiting an apoptotic morphology. This indicates that miR-181a-5p/AgNPs can further inhibit proliferation and induce apoptosis of oral cancer cells compared to AgNPs alone (Figure 5I and J).

Prediction and Screening of Target Genes and Construction of the miR-181a-5p/Target Gene Network

To further study its molecular mechanisms, the target gene of miR-181a-5p was predicted and screened. The interaction network of miR-181a-5p and its main targets, validated in previous studies, is shown in Figure 6A. BCL2 was selected as a key candidate target gene for further research.

miR-181a-5p Binds to BCL2 3′-UTR

We found that BCL2 is a potential target gene of miR-181a-5p and screened their binding sites (Figure 6B). The dual-luciferase reporter assay showed that, in the miR-181a-5p mimic group, the luciferase activity of the wild-type BCL2 3′-

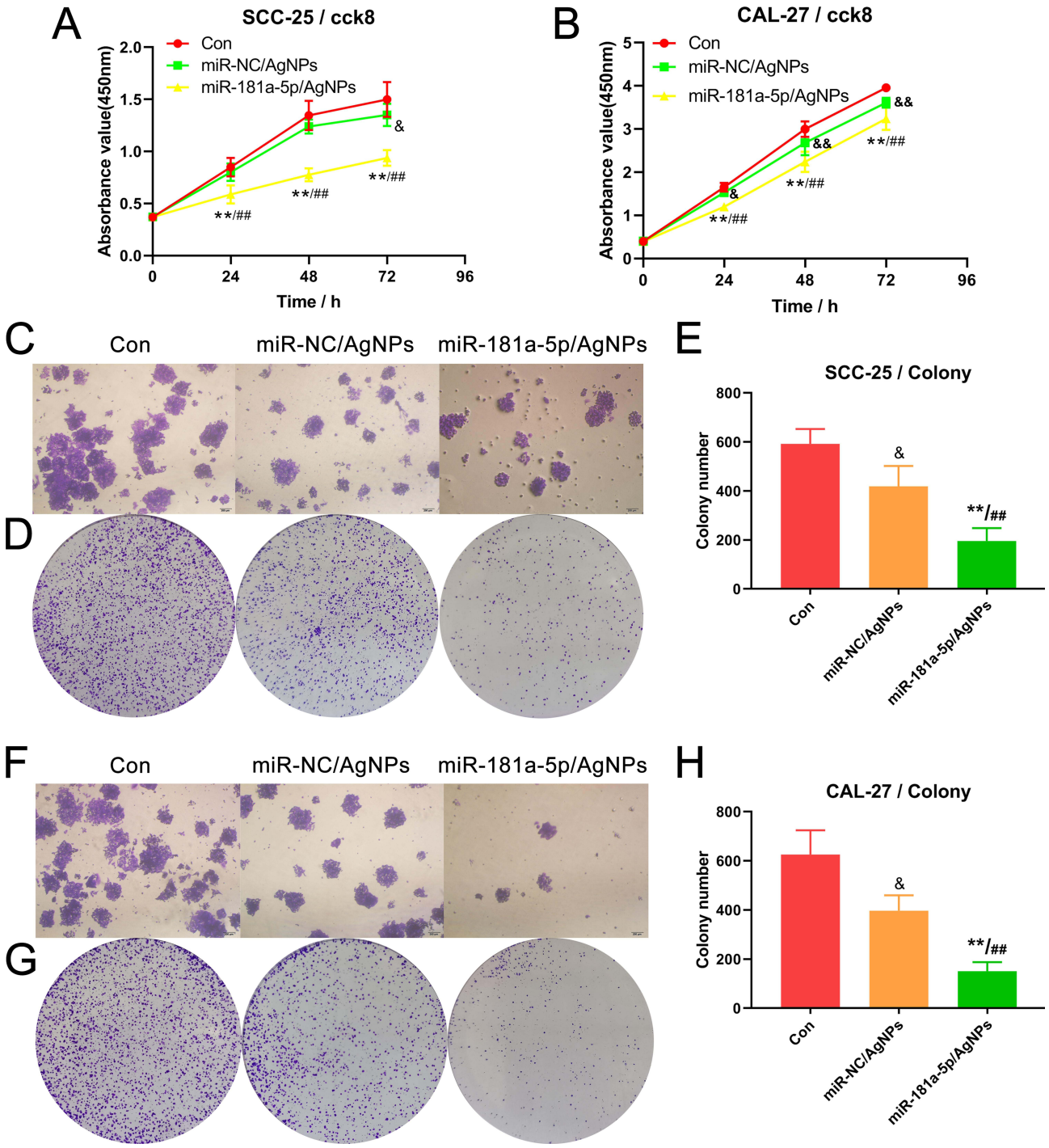

Figure 4 Detection of proliferation and colony formation in oral cancer cell lines. (**A**) Proliferation detection in the SCC-25 cell line. (**B**) Proliferation detection in the CAL-27 cell line. (**C**). Detection of colony formation in the SCC-25 cell line (microscopic images). (**D**). Detection of colony formation in the SCC-25 cell line (under the digital camera). (**E**). Statistics of colony formation in the SCC-25 cell line. (**F**) Detection of colony formation in the CAL-27 cell line (microscopic images). (**G**). Detection of colony formation in the CAL-27 cell line (under the digital camera). (**H**) Statistics of colony formation in the CAL-27 cell line.

Notes:**miR-181a-5p/AgNPs group compared with the Con group, $P < 0.01$; ##miR-181a-5p/AgNPs group compared with the miR-NC/AgNPs group, $P < 0.01$; and: miR-NC/AgNPs group compared with the Con group, $P < 0.05$; andand: miR-NC/AgNPs group compared with the Con group, $P < 0.01$.

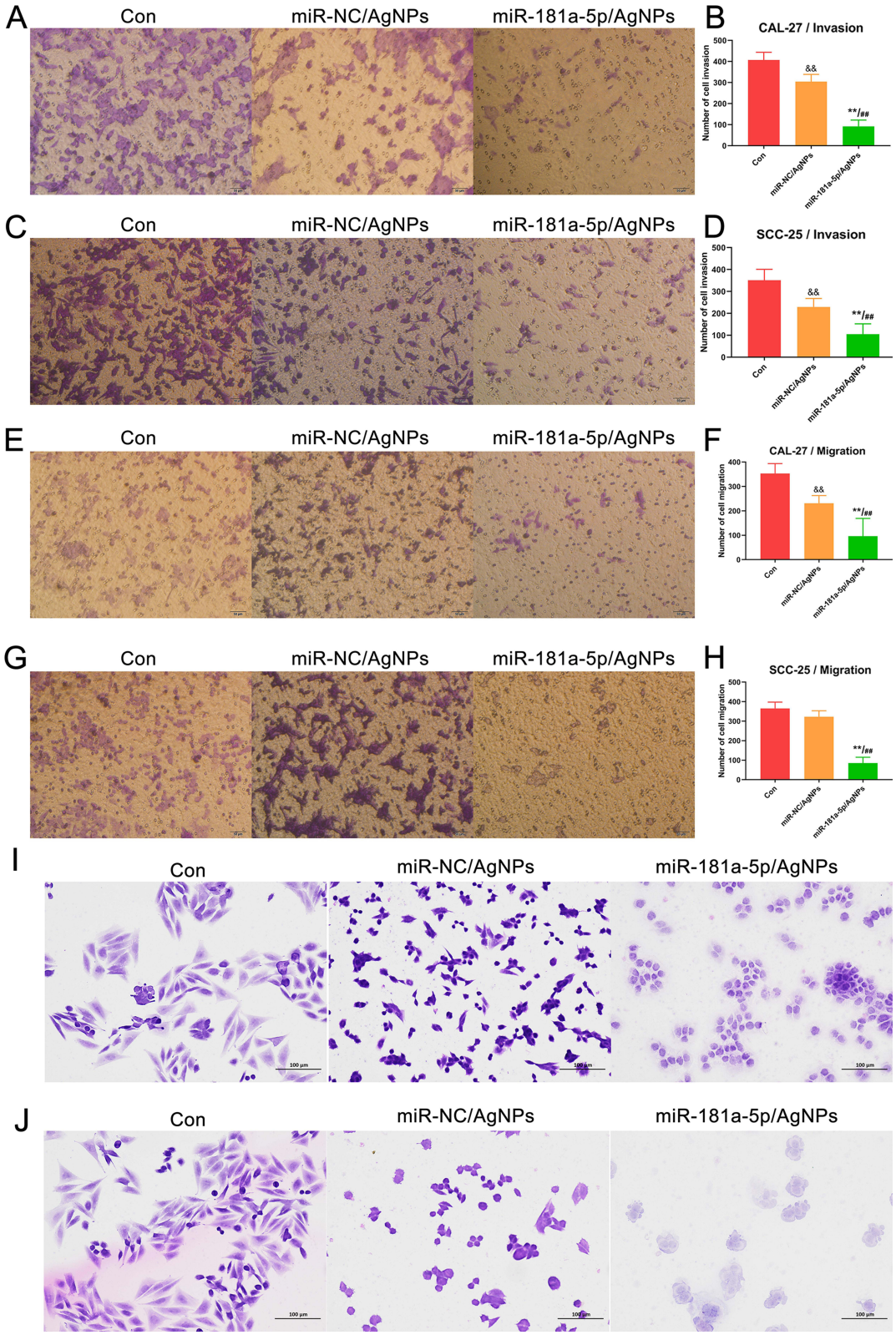

Figure 5 Invasion, migration, and pathological detection in oral cancer cell lines. (**A**) Detection of invasion in the CAL-27 cell line. (**B**) Statistics of invasion results in the CAL-27 cell line. (**C**) Detection of invasion in the SCC-25 cell line. (**D**) Statistics of invasion results in the SCC-25 cell line. (**E**) Detection of migration in the CAL-27 cell line. (**F**) Statistics of migration results in the CAL-27 cell line. (**G**) Detection of migration in the SCC-25 cell line. (**H**) Statistics of migration results in the SCC-25 cell line. (**I**) Morphology and pathological changes of the CAL-27 cell line. (**J**) Morphology and pathological changes of the SCC-25 cell line.

Notes: **: miR-181a-5p/AgNPs group compared with the Con group, $P < 0.01$; ##: miR-181a-5p/AgNPs group compared with the miR-NC/AgNPs group, $P < 0.01$; andand: miR-NC/AgNPs group compared with the Con group, $P < 0.01$.

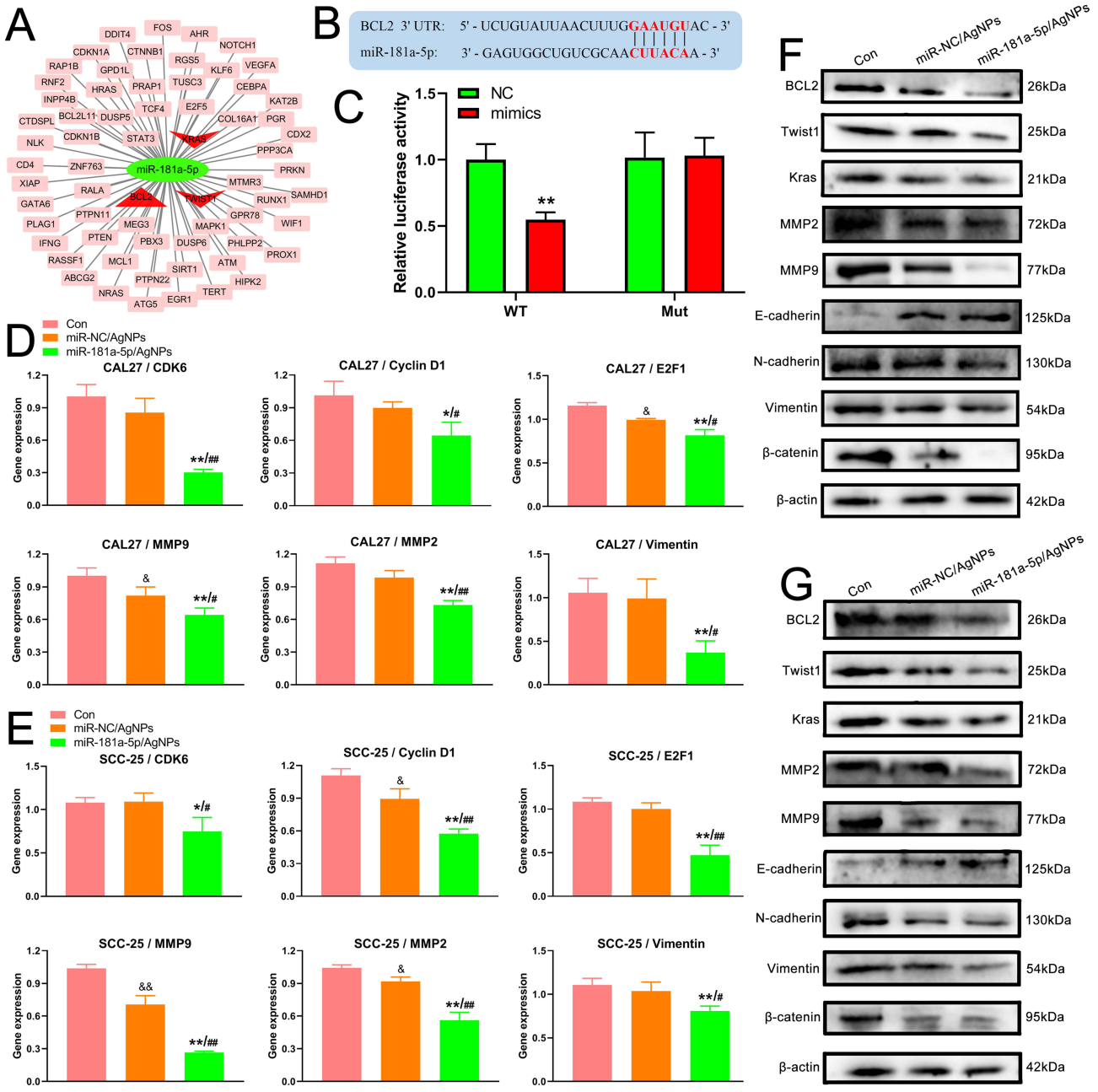

Figure 6 Prediction and validation of target genes, as well as detection of downstream genes and proteins. (**A**) Networks of miR-181a-5p and its main target genes. (**B**) Binding sites of miR-181a-5p to BCL2. (**C**) Validation of miR-181a-5p binding to BCL2 using dual luciferase reporter assay. (**D**) Detection of downstream gene expression in the CAL-27 cell line. (**E**) Detection of downstream gene expression in the SCC-25 cell line. (**F**) Detection of target and downstream protein expression in the CAL-27 cell line. (**G**). Detection of target and downstream protein expression in the SCC-25 cell line.

Notes: *: miR-181a-5p/AgNPs group compared with the Con group, $P < 0.05$; **: miR-181a-5p/AgNPs group compared with the Con group, $P < 0.01$; #: miR-181a-5p/AgNPs group compared with the miR-NC/AgNPs group, $P < 0.05$; ##: miR-181a-5p/AgNPs group compared with the miR-NC/AgNPs group, $P < 0.01$; and: miR-NC/AgNPs group compared with the Con group, $P < 0.05$; andand: miR-NC/AgNPs group compared with the Con group, $P < 0.01$.

UTR (Wt-BCL2) was significantly inhibited. However, there were no significant changes in the miR-181a-5p mimics NC and mutant BCL2 3′-UTR (Mut-BCL2) groups (Figure 6C).

The Effects on Tumorigenesis-Related Genes and Proteins

To better explore the molecular mechanisms of tumor suppression, we detected the expression of the target gene and related downstream genes. The results indicated that the target genes *BCL2, Kras*, and *Twist1* were significantly

downregulated in the miR-181a-5p/AgNPs group. Meanwhile, the downstream genes *Cyclin D1, CDK6, E2F1, MMP9, MMP2*, and *Vimentin* also had significantly lower expression levels in the miR-181a-5p/AgNPs group in the two oral cancer cell lines (Figure 3B, Figure 6D and E).

Moreover, we detected the related target and downstream protein expression in the cell lines. The results showed that treatment with AgNPs and miR-181a-5p/AgNPs significantly inhibited the expression of BCL2, Twist1, Kras, MMP2, MMP9, N-cadherin, Vimentin, and β-catenin, but promoted the expression of the E-cadherin protein. The promotion and inhibition effects of miR-181a-5p/AgNPs were more significant (Figure 6F and G). Our findings suggest that miR-181a-5p/AgNPs may inhibit oral cancer development by suppressing target genes and proteins as well as the downstream β-catenin signaling pathway.

Analysis of Tumor Volume and Weight

In vivo assays showed that delivery of miR-181a-5p using AgNPs as nanocarriers effectively inhibited the growth of transplanted tumors (Figure 7A and B). Additionally, we measured the weight of the isolated tumor, and the results indicated that the tumor weight in the AgNPs (AgNPs/NC) group was significantly lower than that in the normal group. Compared with the control group and AgNPs group, the tumor weight of the nanocomposite group was significantly reduced (Figure 7C).

Furthermore, compared with the control group, after 21 days of treatment, the tumor weight of the AgNPs group decreased by about 40%, while the group treated with miR-181a-5p/AgNPs composite showed a 76% reduction in tumor weight (Figure 7D). In the analysis of tumor growth inhibition rate, compared with the control group, the tumor volume decreased by about 37% in the AgNPs group and 75% in the miR-181a-5p/AgNPs group (Figure 7E).

Pathological Examination

To further evaluate the therapeutic effects of the AgNPs and the nanocomposite, HE and immunohistochemical staining were performed. The results showed that the tumors in the control group were composed of masses of malignant cells. The tumor tissue in the control group contained rich blood vessels, with the tumor cells being primarily spindle-shaped and exhibiting an elevated nuclear-to-cytoplasmic ratio. Some tumor cells showed an insular or nested distribution. However, mice treated with nanosilver (AgNPs) or the composite (miR-181a-5p/AgNPs) showed significantly reduced tumor malignancy. Some cells underwent apoptosis, and tissues contained necrotic cell clusters accompanied by nuclear chromatin condensation, fragmentation, and cell shrinkage, with their tumors being significantly disrupted. Additionally, the tumors in the AgNPs group were damaged to a certain extent compared to the PBS control group, but the damage was weaker than that in the composite group (Figure 7F).

At the same time, we assessed the degree of cell proliferation in tumor tissue using Ki67 expression levels. Immunohistochemistry showed that, compared to the control group, the AgNPs and miR-181a-5p/AgNPs-treated groups had a lower number of Ki67-positive cells. The number of Ki67-positive cells and staining area were lowest in the miR-181a-5p/AgNPs-treated group. These results indicated that the proliferation of tumors was significantly inhibited in the treated groups, with the inhibition being more effective in the miR-181a-5p/AgNPs-treated group (Figure 7G).

Body Weight Detection and Evaluation of Weight Inhibition Rate

To examine the toxicity of the nanocomposite, we monitored the body weight of the nude mice. As shown in Figure 8A, there were no significant changes in body weight among the nude mice across treatment groups throughout the experiment. In Figure 8B, the analysis of weight inhibition rate in the treatment group revealed that nanosilver and composites did not exert a significant inhibitory effect on the body weight of the nude mice. Both Figure 8A and B indicate that the nanosilver carrier and composite have no significant toxicity towards mice during the treatment process, demonstrating their favorable biocompatibility.

Detection of Organ Coefficient

To further investigate the toxicity effect of the nanocomposite, the organ coefficients of the heart, liver, spleen, lung, and kidney for the three groups were analyzed. As shown in Table 3, no significant organ damage or abnormalities were

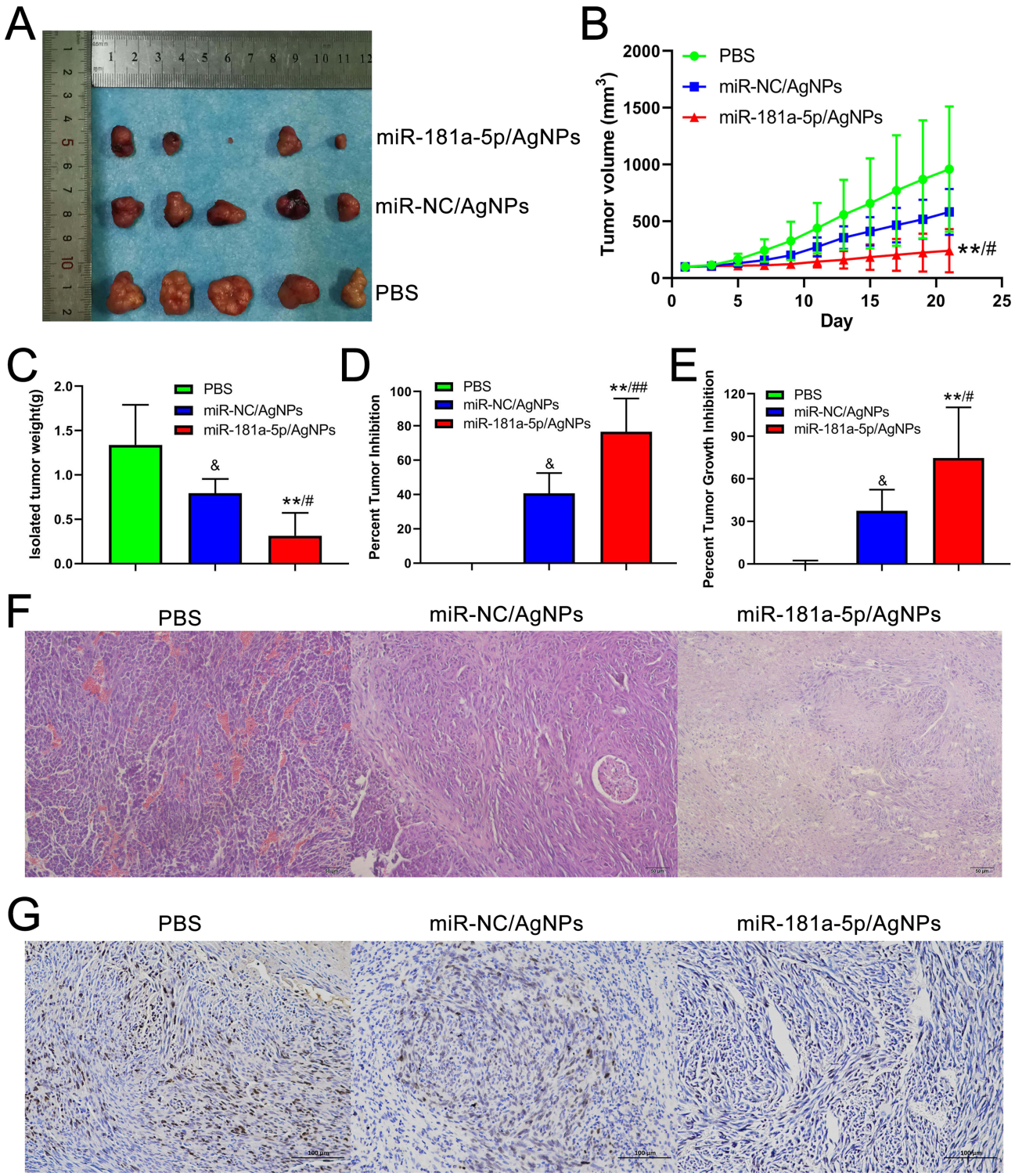

Figure 7 Validation of tumor-suppressing effects in a xenograft model. (**A**) Isolated tumors from the xenograft model. (**B**) Tumor growth curves. (**C**) Weight statistics for isolated tumors. (**D**). Statistics on tumor inhibition rate. (**E**). Statistics on tumor growth inhibition rate. (**F**). HE staining of isolated tumors. (**G**). Immunohistochemical analysis of Ki67 in the isolated tumors.

Notes: **: miR-181a-5p/AgNPs group compared with the Con group, $P < 0.01$; #: miR-181a-5p/AgNPs group compared with the miR-NC/AgNPs group, $P < 0.05$; ##: miR-181a-5p/AgNPs group compared with the miR-NC/AgNPs group, $P < 0.01$; and: miR-NC/AgNPs group compared with the Con group, $P < 0.05$.

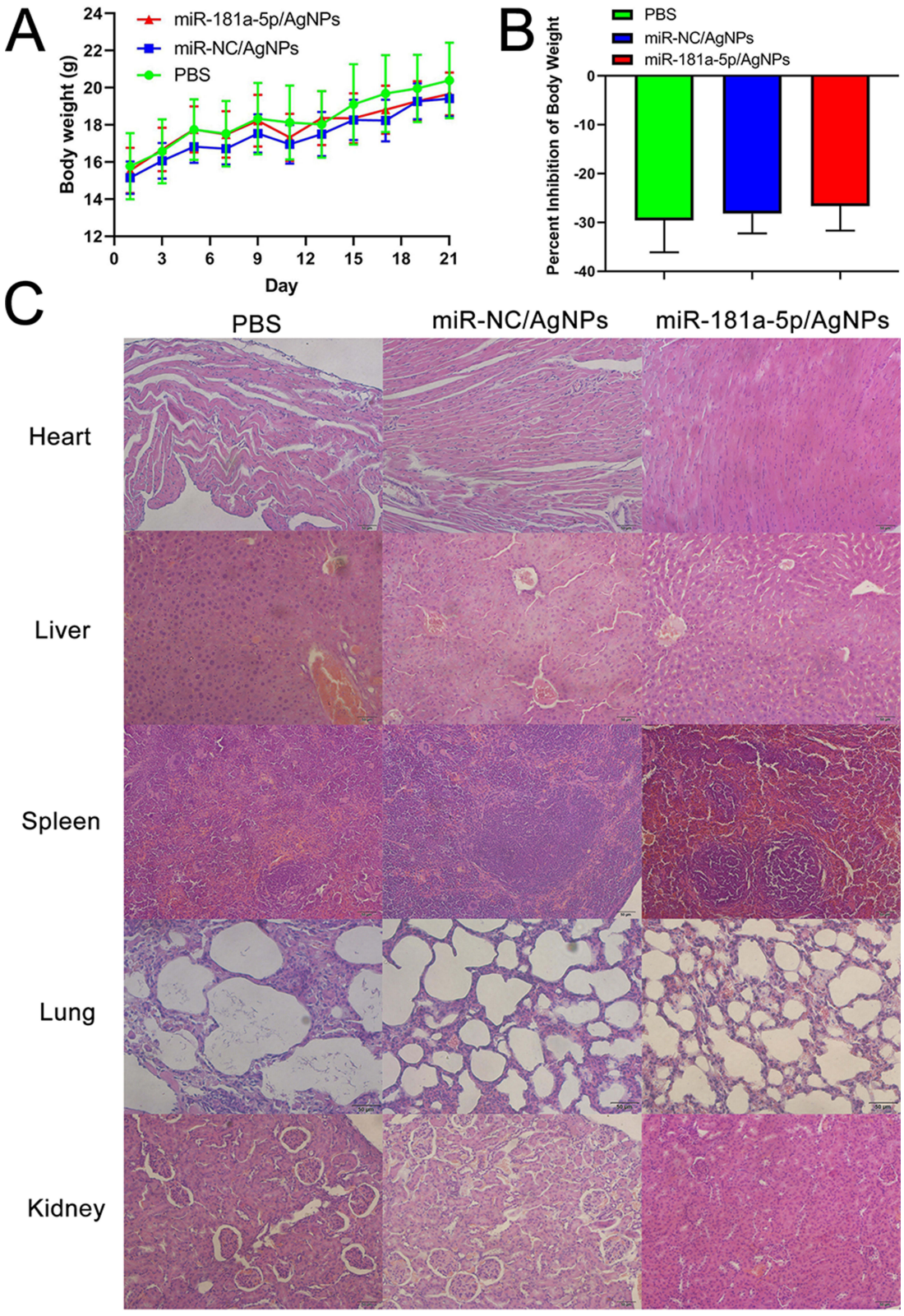

Figure 8 In vivo safety evaluation. (**A**) Weight change curves in nude mice with xenograft tumors. (**B**) Analysis of body weight inhibition rate. (**C**) HE staining of main organs (heart, liver, spleen, lung, and kidney) in nude mice with xenograft tumors.

Table 3 Organ Coefficients of Nude Mice

Organ	PBS	AgNPs	miR-181a-5p/AgNPs
Heart	0.5788±0.1948	0.5405±0.0348	0.5501±0.0198
Liver	8.0120±0.3496	7.9315±1.0339	7.8516±1.1680
Spleen	1.8694±0.1560	1.8440±0.2255	1.7185±0.1849
Lungs	0.8609±0.0629	0.9817±0.2457	0.7887±0.0286
Kidney	1.5076±0.1323	1.5230±0.1778	1.5597±0.0795

observed in all groups, and no significant difference was detected in the organ coefficients between the three groups. The results indicated that the AgNPs and miR-181a-5p/AgNPs have good organ compatibility.

Pathological Changes in the Main Organs

After dissection, observation with the naked eye revealed no discernible differences in the organs of all three groups. Moreover, we further assessed potential toxicity toward major organs (heart, liver, spleen, lung, and kidney) by HE staining. The results revealed that in the three groups, the structure of the main organs was intact, and no obvious organ damage or abnormalities were observed. These findings were consistent with the results of body weight and organ coefficients, indicating that the miR-181a-5p/AgNPs composite has no obvious toxicity to the main organs. This further reveals that the nanocomposite has a good safety profile (Figure 8C).

Neurotoxicity Assessments

To evaluate the biosafety of AgNPs and AgNP-miRNA, we performed toxicity assessments on neuronal cells SH-SY5Y and HT22. The results indicate that neither AgNPs nor miR-181a-5p/AgNPs significantly affected cell viability (Supplementary Figures 3 and 4) or oxidative stress levels (Supplementary Figures 5 and 6) in these neuronal cells. This suggests that, under our synthesis conditions, they exhibit minimal neurotoxicity.

Molecular Mechanism Validation In Vivo

Immunohistochemical staining was employed to validate protein expression in the three groups. As illustrated in Figure 9, the miR-181a-5p/AgNPs group exhibited significantly higher E-cadherin expression compared to the other groups. Additionally, the expression of BCL2, Twist1, β-catenin, Vimentin, N-cadherin, MMP2, and MMP9 was notably lower in the miR-181a-5p/AgNPs group compared to the other groups. These proteins also showed a decreasing trend in the AgNPs group; however, this trend was more pronounced in the miR-181a-5p/AgNPs group. Thus, the tumor-suppressive effect of the miR-181a-5p/AgNPs group was more prominent, consistent with our in vitro validation results in oral cancer cells, indicating superior tumor suppressive efficacy of miR-181a-5p/AgNPs nanocomplexes over single nanomedicines. Our in vivo findings further demonstrated that miR-181a-5p/AgNPs could inhibit oral cancer by suppressing the target protein and downstream β-catenin signaling pathway, aligning with our in vitro findings.

Discussion

Oral cancer presents a significant global health challenge with a low survival rate and poor prognosis. Annually, over 400,000 new cases are diagnosed worldwide, highlighting its widespread impact.[1] Despite advancements in clinical diagnosis and therapy, the prognosis for oral cancer remains bleak.[38] One contributing factor is the inefficacy and toxicity of current treatment modalities.[39] Additionally, the molecular mechanisms underlying oral cancer pathogenesis remain poorly understood.[40] Therefore, there is an urgent need to develop effective treatment strategies and elucidate the underlying pathogenesis of oral cancer.

Accumulating evidence suggests that miRNAs play a pivotal role in the occurrence and progression of oral cancer.[7,39,41] Research has underscored the essential role of miRNAs in oral cancer onset and progression, highlighting their potential as crucial regulatory molecules in treatment. Notably, miRNAs have shown promise as effective treatment agents for tumors without causing toxicity to normal cells.[42–44] Consequently, miRNAs are considered a promising

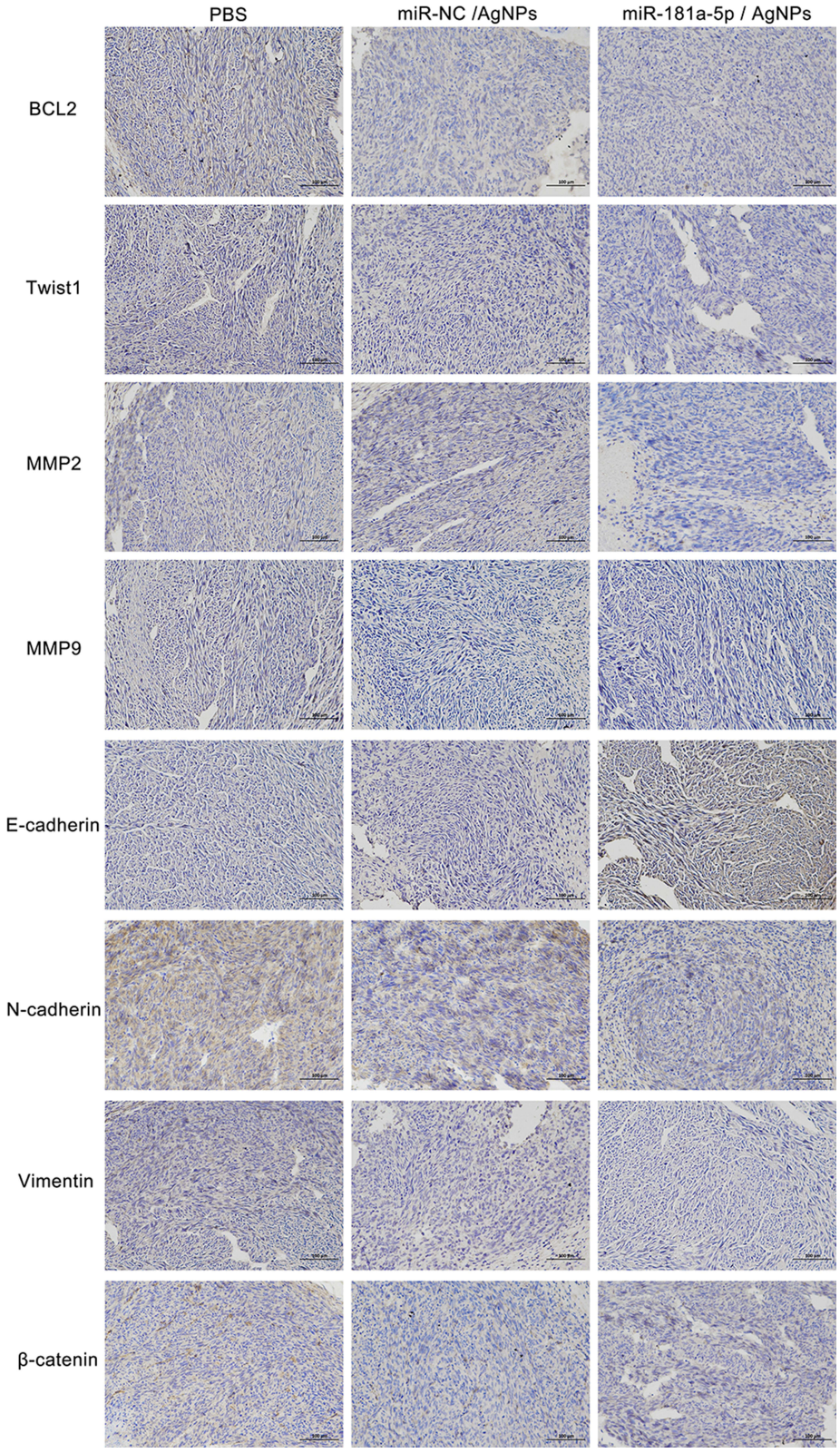

Figure 9 Immunohistochemical detection of target and downstream proteins in isolated tumors.

option for gene therapy. However, the application of miRNA-based gene therapy faces numerous obstacles, including low cell uptake, immunogenicity, kidney clearance, nuclease degradation, poor internal release, and adverse side effects associated with high-dose therapy.[45,46] Various approaches, such as probes and miRNA delivery vectors based on adenovirus and lentivirus, have been explored to overcome these challenges. Despite their potential, these methods also present biological toxicity and side effects.[47,48] Current research efforts predominantly focus on utilizing nanodrugs and nanocarriers to treat malignant tumors.[39,49,50] Substantial attention has been directed towards the development of nanocarriers to enhance miRNA delivery efficacy and minimize associated challenges.

Traditional miRNA delivery methods primarily include lipid-based transfection and chemically modified miRNAs. While these methods are commonly employed in preliminary in vitro cell experiments, they have limitations for further in vivo therapeutic research.[51] Lipid-based miRNA delivery involves encapsulating miRNA within liposome particles to enhance stability and bioavailability, facilitating cellular entry. However, liposomes may undergo rapid degradation by in vivo enzymes, leading to premature miRNA release and degradation before reaching target cells.[26] Additionally, the lack of sufficient targeting specificity results in broad distribution throughout normal tissues, causing unnecessary side effects.[26,51] Some liposome materials may trigger immune responses, leading to inflammation or other adverse reactions.[26,51] Chemical modification alters miRNA structure to enhance cellular uptake and stability. However, this process is complex, requiring specialized reagents and equipment, which leads to higher production costs. At the same time, not all miRNAs can be effectively modified. Moreover, chemically modified miRNAs may lose their biological activity and undergo engulfment and degradation by endosomes during in vivo therapy.[51]

Because cancer cells exhibit a high permeability and retention effect, nanosilver can readily enter and accumulate in target cancer cells. Moreover, in clinical medicine, nanosilver finds utility in various applications such as antimicrobial excipients, surgical sutures, heart valves, and targeting agents.[52] Several studies have highlighted the potential of nanosilver in the early detection and clinical diagnosis of cancers including colorectal, gastric, cervical, esophageal, and prostate cancer.[33–36] Consequently, nanosilver has emerged as an effective drug delivery system owing to its intrinsic properties.[53,54] Its excellent antibacterial properties further allow for the prevention of contamination during the transfection process, providing a significant advantage over conventional carriers.[48,49] The outstanding antibacterial properties of nanosilver effectively prevent contamination during the transfection process, offering a significant advantage over conventional carriers when used as cell transfection vectors.[53,54] Through the utilization of common raw materials and refined synthesis methods, we have addressed potential adverse environmental impacts, high preparation costs, and the complexity of synthesis and production processes associated with nanodrugs. Consequently, our nanocomposite has become more convenient and safe.

Notably, the synthesis process of nanosilver in our research does not involve the use of toxic chemical reagents, resulting in minimal environmental impact and positioning it as a novel environmentally friendly transfection agent. Moreover, compared to other commercially available transfection carriers, the multifaceted characteristics of the nanocarrier delivery system can be tailored according to experimental requirements. Lastly, the small size and large specific surface area of nanocarriers enable them to circulate longer in vivo, effectively enhancing therapeutic outcomes.[53,54]

In our study, AgNPs were successfully prepared using AA as a reducing agent. Co-incubation of miR-181a-5p and AgNPs solutions yielded miR-181a-5p/AgNPs nanocomplexes. Characterization by fluorescence development demonstrated the excitation of AgNPs to fluoresce, with bright intracellular green fluorescence observed in tumor cells. Furthermore, the miR-181a-5p/AgNPs composites exhibited high transfection efficiency and effectively protected miRNA from degradation by RNase and serum.

To elucidate the complex's biological mechanism in regulating oral cancer cells, we utilized miR-181a-5p/AgNPs nanocomposites to deliver miR-181a-5p into oral cancer cells. In vitro functional assays revealed the inhibitory effects of miR-181a-5p on cell proliferation, colony formation, migration, and invasion. Simultaneously, to better explore the role of miR-181a-5p in tumor suppression in vivo, we constructed a tumor xenograft animal model. The results showed that both nanosilver and the composite significantly inhibited tumor growth in vivo, with the composite exhibiting superior efficacy to nanosilver alone. We found that miR-181a-5p/AgNPs not only efficiently delivered miR-181a-5p but also showed excellent antitumor activity both in vitro and in vivo. These findings suggest the potential of miR-181a-5p/AgNPs nanocomposites as oral cancer suppressors.

Hemolysis tests and xenograft tumor model evaluations demonstrated favorable biosafety profiles of both AgNPs and miR-181a-5p/AgNPs in vivo and in vitro. Additionally, neurotoxicity assessments revealed almost no significant neurotoxicity. We speculate that several factors may account for the absence of significant neurotoxicity observed: Firstly, our comprehensive treatment approach employed low single doses that were insufficient to induce neurotoxicity. Secondly, the brief duration of administration further limited the cumulative dose of nanomedicine, preventing damage. Furthermore, to comprehensively evaluate the neurotoxicity of AgNPs and miR-181a-5p/AgNPs, we intend to employ animal models in subsequent research to investigate their effects on behavior, brain myelination, cerebral pathological alterations, and changes in oxidative stress levels within the nervous system.

Our previous animal models and functional verification of oral cancer cell lines have demonstrated the promising antitumor effects of miR-181a-5p. Similarly, Shin KH reported a downregulation of miR-181a-5p in oral cancer.[11] The functional analysis by Liu et al showed a significant downregulation of miR-181a in stable cisplatin-resistant oral cancer cell lines, with the miR-181a-Twist1 pathway identified as reversing chemical resistance and inhibiting EMT.[12] The high expression of miR-181a-5p significantly delays the development of NPC,[17] while also inducing cell senescence and shortening cell lifespan.[18] These findings align with our results, indicating the potential tumor suppressor function of miR-181a-5p across various contexts.

In the present study, we discovered that miR-181a-5p directly targets the 3'-UTR region of BCL2 to inhibit its expression. Overexpression of miR-181a-5p significantly reduced the expression of Twist1, Kras, β-catenin, MMP2, MMP9, N-cadherin, and Vimentin, while increasing the expression of E-cadherin. Increased BCL2 expression in tumor vessels has been associated with patients' metastasis status in head and neck squamous cell carcinoma, suggesting its role in promoting tumor angiogenesis, vascular leakage, and metastasis.[55] In oral cancer tissue, BCL2 interacts with Twist1, correlating with pathological grade and poor prognosis.[56] In our study, miR-181a-5p/AgNPs nanocomplexes notably decreased the expression of the target gene BCL2, consequently affecting Twist1 expression and the activation of the β-catenin signaling pathway. This inhibition led to decreased expression of invasion-related genes MMP2 and MMP9, EMT-related genes N-cadherin and Vimentin, and increased expression of E-cadherin. Therefore, the nanocomposites suppress the β-catenin signaling pathway activation through the miR-181a-5p/BCL2/Twist1 axis, inhibiting the occurrence and progression of oral cancer.

This study successfully synthesized nanosilver loaded with anti-cancer miRNA to form a nanocomposite, thoroughly investigating its in vivo and in vitro anti-cancer mechanisms and biosafety. Additionally, research was conducted on the neurotoxicity of nanosilver and the nanocomposite. Subsequent research will utilize appropriate animal models for in-depth studies on the neurotoxicity of AgNPs and the composites within living organisms, investigating their potential impact on the nervous system, brain, and long-term biosafety profile. Challenges may arise in future clinical applications of AgNPs/miRNA, including the impact of the tumor microenvironment's heterogeneity and complexity on nanocomposite targeting precision and stability, as well as large-scale production and cost control. Ongoing research and innovation are essential to overcome these challenges and unleash the potential of nanotechnology in cancer treatment. In the future, it is imperative to strengthen interdisciplinary collaboration to develop more efficient, stable, and safe nanocomposite drugs, as well as to explore the applications of nanotechnology in cancer immunotherapy and gene therapy.

Conclusion

We successfully synthesized nanosilver with uniform distribution, capable of emitting fluorescence upon excitation, exhibiting excellent biocompatibility, and ensuring high safety. Utilizing this nanosilver as a base, we prepared a nanocomposite loaded with the tumor suppressor gene miR-181a-5p. The resulting nanocomposite effectively inhibits the growth and progression of oral cancer both in vitro and in vivo, partially attributed to its suppression of the β-catenin signaling pathway. These effects demonstrate synergy that may be challenging for a single drug to achieve in treatment. In vivo treatment and histopathological analysis revealed a significant reduction in transplanted tumor growth without apparent toxicity to other organs. Overall, this study presents novel options for the clinical prevention and treatment of oral cancer, focusing on modulating gene expression through non-coding RNAs and utilizing nanodrug therapy.

Data Sharing Statement

The data that support the findings of this study are available from the corresponding author upon reasonable request.

Acknowledgments

This work was supported by the National Natural Science Foundation of China (31772551 and 31970513), the Shanxi Scholarship Council of China (2021-086), Special fund for Science and Technology Innovation Teams of Shanxi Province (202204051002032), the Central Government's Guide to Local Science and Technology Development Found (YDZJSX2022A060), and the Natural Science Foundation of Shanxi Province (20210302124093). We would like to thank Editage (www.editage.cn) for English language editing.

Disclosure

The authors report no conflicts of interest in this work.

References

1. Sung H, Ferlay J, Siegel RL. et al. Global Cancer Statistics 2020: GLOBOCAN Estimates of Incidence and Mortality Worldwide for 36 Cancers in 185 Countries. *Ca Cancer J Clin*. 2021;71(3):209–249. doi:10.3322/caac.21660
2. Manikandan M, Deva Magendhra Rao AK, Arunkumar G, et al. Oral squamous cell carcinoma: microRNA expression profiling and integrative analyses for elucidation of tumourigenesis mechanism. *Mol Cancer*. 2016;15(1):28. doi:10.1186/s12943-016-0512-8
3. Zhang GM, Nie SC, Xu ZY, et al. Advanced Polymeric Nanoagents for Oral Cancer Theranostics: a Mini Review. *Front Chem*. 2022;10:927595. doi:10.3389/fchem.2022.927595
4. Sadasivam S, Subramanian R. A perspective on challenges and opportunities in characterizing oral cancer stem cells. *Front Biosci*. 2020;25 (6):1011–1021. doi:10.2741/4845
5. Ling Z, Cheng B, Tao X. Epithelial-to-mesenchymal transition in oral squamous cell carcinoma: challenges and opportunities. *Intl J Cancer*. 2021;148(7):1548–1561. doi:10.1002/ijc.33352
6. Xu GQ, Li LH, Wei JN, et al. Identification and profiling of microRNAs expressed in oral buccal mucosa squamous cell carcinoma of Chinese hamster. *Sci Rep*. 2019;9(1):15616. doi:10.1038/s41598-019-52197-3
7. Wang X, Nie X, Xu G, et al. miR-450b promotes cell migration and invasion by inhibiting SERPINB2 in oral squamous cell carcinoma. *Oral Dis*. 2022. doi:10.1111/odi.14407
8. Wang X, Chang K, Gao J, et al. MicroRNA-504 functions as a tumor suppressor in oral squamous cell carcinoma through inhibiting cell proliferation, migration and invasion by targeting CDK6. *Int J Biochem Cell Biol*. 2020;119:105663. doi:10.1016/j.biocel.2019.105663
9. Huang GZ, Wu QQ, Zheng ZN, Shao TR, Lv XZ. Identification of Candidate Biomarkers and Analysis of Prognostic Values in Oral Squamous Cell Carcinoma. *Front Oncol*. 2019;9:1054. doi:10.3389/fonc.2019.01054
10. Xu G, Yang Y, Yang J, et al. Screening and identification of miR-181a-5p in oral squamous cell carcinoma and functional verification in vivo and in vitro. *BMC Cancer*. 2023;23(1):162. doi:10.1186/s12885-023-10600-3
11. Shin KH, Bae SD, Hong HS, Kim RH, Kang MK, Park NH. miR-181a shows tumor suppressive effect against oral squamous cell carcinoma cells by downregulating K-ras. *Biochem Biophys Res Commun*. 2011;404(4):896–902. doi:10.1016/j.bbrc.2010.12.055
12. Liu M, Wang J, Huang H, Hou J, Zhang B, Wang A. miR-181a-Twist1 pathway in the chemoresistance of tongue squamous cell carcinoma. *Biochem Biophys Res Commun*. 2013;441(2):364–370. doi:10.1016/j.bbrc.2013.10.051
13. Ju R, Huang Y, Guo Z, et al. The circular RNAs differential expression profiles in the metastasis of salivary adenoid cystic carcinoma cells. *Mol Cell Biochem*. 2021;476(2):1269–1282. doi:10.1007/s11010-020-03989-z
14. He Q, Zhou X, Li S, et al. MicroRNA-181a suppresses salivary adenoid cystic carcinoma metastasis by targeting MAPK-Snai2 pathway. *BBA*. 2013;1830(11):5258–5266. doi:10.1016/j.bbagen.2013.07.028
15. Kumar P, Kumawat RK, Uttam V, et al. The imminent role of microRNAs in salivary adenoid cystic carcinoma. *Transl Oncol*. 2023;27:101573. doi:10.1016/j.tranon.2022.101573
16. Hao YR, Zhang DJ, Fu ZM, Guo YY, Guan GF. Long non-coding RNA ANRIL promotes proliferation, clonogenicity, invasion and migration of laryngeal squamous cell carcinoma by regulating miR-181a/Snai2 axis. *Regener Ther*. 2019;11:282–289. doi:10.1016/j.reth.2019.07.007
17. Liu J, Zhu M, Tang Q. Human umbilical cord mesenchymal stem cells-derived exosomal microRNA-181a retards nasopharyngeal carcinoma development by mediating KDM5C. *J Cancer Res Clin Oncol*. 2021;147(10):2867–2877. doi:10.1007/s00432-021-03684-6
18. Gerasymchuk M, Cherkasova V, Kovalchuk O, Kovalchuk I. The Role of microRNAs in Organismal and Skin Aging. *Int J Mol Sci*. 2020;21 (15):5281. doi:10.3390/ijms21155281
19. Smith MH, Lyon LA. Multifunctional nanogels for siRNA delivery. *Acc Chem Res*. 2012;45(7):985–993. doi:10.1021/ar200216f
20. Juliano R, Alam MR, Dixit V, Kang H. Mechanisms and strategies for effective delivery of antisense and siRNA oligonucleotides. *Nucleic Acids Res*. 2008;36(12):4158–4171. doi:10.1093/nar/gkn342
21. Kurreck J. RNA interference: from basic research to therapeutic applications. *Angew Chem*. 2009;48(8):1378–1398. doi:10.1002/anie.200802092
22. Abdolahpur Monikh F, Chupani L, Vijver MG, Vancová M, Peijnenburg W. Analytical approaches for characterizing and quantifying engineered nanoparticles in biological matrices from an (eco)toxicological perspective: old challenges, new methods and techniques. *Sci Total Environ*. 2019;660:1283–1293. doi:10.1016/j.scitotenv.2019.01.105
23. Shehata AM, Salem FMS, El-Saied EM, El-Rahman SS A, Mahmoud MY, Noshy PA. Evaluation of the Ameliorative Effect of Zinc Nanoparticles against Silver Nanoparticle-Induced Toxicity in Liver and Kidney of Rats. *Biol Trace Elem Res*. 2022;200(3):1201–1211. doi:10.1007/s12011-021-02713-2

24. Chugh H, Sood D, Chandra I, Tomar V, Dhawan G, Chandra R. Role of gold and silver nanoparticles in cancer nano-medicine. *Artif Cells Nanomed Biotechnol*. 2018;46(sup1):1210–1220. doi:10.1080/21691401.2018.1449118
25. Jha M, Shimpi NG. Green synthesis of zero valent colloidal nanosilver targeting A549 lung cancer cell: in vitro cytotoxicity. *J Genet Eng Biotechnol*. 2018;16(1):115–124. doi:10.1016/j.jgeb.2017.12.001
26. Yang Y, Li J, Liu F, et al. Systemic Delivery of siRNA via LCP Nanoparticle Efficiently Inhibits Lung Metastasis. *Mol Ther*. 2012;20(3):609–615. doi:10.1038/mt.2011.270
27. Cameron SJ, Hosseinian F, Willmore WG. A Current Overview of the Biological and Cellular Effects of Nanosilver. *Int J Mol Sci*. 2018;19 (7):2030. doi:10.3390/ijms19072030
28. SH S, MK Y. The effect of nano-silver on the activation of nasal polyp epithelial cells by Alternaria, Der P1 and staphylococcal enterotoxin B. *Int Immunopharmacol*. 2011;11(11):1691–1696. doi:10.1016/j.intimp.2011.05.028
29. Z Y, L A, Z Y, et al. Bacteria-Targeting Nanosilver-Based Antibacterial Drugs for Efficient Treatment of Drug-Resistant Bacterial-Infected Keratitis. *Macromol Rapid Commun*. 2023;44(23):e2300379. doi:10.1002/marc.202300379
30. N I, V V, J Z, N S. Known data on the effectiveness of silver nano particles on root canal disinfection. *Bioinformation*. 2021;17(1):218–222. doi:10.6026/97320630017218
31. Oladipo AO, Unuofin JO, Lebelo SL, Msagati TAM. Phytochemical-Stabilized Platinum-Decorated Silver Nanocubes INHIBIT Adenocarcinoma Cells and Enhance Antioxidant Effects by Promoting Apoptosis via Cell Cycle Arrest. *Pharmaceutics*. 2022;14(11):2541. doi:10.3390/pharmaceutics14112541
32. Nguyen MP, Pham DP, Kim D. Oxidative Stress-Induced Silver Nano-Carriers for Chemotherapy. *Pharmaceuticals*. 2022;15(12):1449. doi:10.3390/ph15121449
33. Orságová Králová Z, Oriňak A, Oriňaková R, et al. Electrochemically deposited silver detection substrate for surface-enhanced Raman spectroscopy cancer diagnostics. *J Biomed Opt*. 2018;23(7):1–11. doi:10.1117/1.jbo.23.7.075002
34. Li D, Feng S, Huang H, et al. Label-free detection of blood plasma using silver nanoparticle based surface-enhanced Raman spectroscopy for esophageal cancer screening. *J Biomed Nanotechnol*. 2014;10(3):478–484. doi:10.1166/jbn.2014.1750
35. Yang L, Zhen SJ, Li YF, Huang CZ. Silver nanoparticles deposited on graphene oxide for ultrasensitive surface-enhanced Raman scattering immunoassay of cancer biomarker. *Nanoscale*. 2018;10(25):11942–11947. doi:10.1039/c8nr02820f
36. Hossain K, Cho HY, Kim KJ, Choi JW. Silver Nanostar Patterned Substrate for Label-Free Characterization of Breast Cancer Cells based on Surface-Enhanced Raman Spectroscopy. *Sci Adv Mater*. 2014;6(11):2491–2495. doi:10.1166/sam.2014.2227
37. Chou CH, Shrestha S, Yang CD, et al. miRTarBase update 2018: a resource for experimentally validated microRNA-target interactions. *Nucleic Acids Res*. 2018;46(D1):D296–D302. doi:10.1093/nar/gkx1067
38. Lee CE, Vincent-Chong VK, Ramanathan A, et al. Collagen Triple Helix Repeat Containing-1 (CTHRC1) Expression in Oral Squamous Cell Carcinoma (OSCC): prognostic Value and Clinico-Pathological Implications. *Int J Med Sci*. 2015;12(12):937–945. doi:10.7150/ijms.11605
39. Ou L, Sun T, Liu M, et al. Efficient miRNA Inhibitor Delivery with Graphene Oxide-Polyethylenimine to Inhibit Oral Squamous Cell Carcinoma. *Int j Nanomed*. 2020;15:1569–1583. doi:10.2147/ijn.s220057
40. Xu G, Wei J, Huangfu B, et al. Animal model and bioinformatics analyses suggest the TIMP1/MMP9 axis as a potential biomarker in oral squamous cell carcinoma. *Mol Carcinog*. 2020;59(11):1302–1316. doi:10.1002/mc.23258
41. Meng X, Lou QY, Yang WY, et al. The role of non-coding RNAs in drug resistance of oral squamous cell carcinoma and therapeutic potential. *Cancer Commun*. 2021;41(10):981–1006. doi:10.1002/cac2.12194
42. Zhang Q, Huang Y, Yang R, Mu J, Zhou Z, Sun M. Poly-antioxidants for enhanced anti-miR-155 delivery and synergistic therapy of metastatic breast cancer. *Biomater Sci*. 2022;10(13):3637–3646. doi:10.1039/d1bm02022f
43. Chitkara D, Mittal A, Mahato RI. miRNAs in pancreatic cancer: therapeutic potential, delivery challenges and strategies. *Adv Drug Delivery Rev*. 2015;81:34–52. doi:10.1016/j.addr.2014.09.006
44. Lennox KA, Behlke MA. Chemical modification and design of anti-miRNA oligonucleotides. *Genet Ther*. 2011;18(12):1111–1120. doi:10.1038/gt.2011.100
45. Cai W, Feng H, Yin L, et al. Bio responsive self-assembly of Au-miRNAs for targeted cancer theranostics. *EBioMedicine*. 2020;54:102740. doi:10.1016/j.ebiom.2020.102740
46. Li J, Tan S, Kooger R, Zhang C, Zhang Y. MicroRNAs as novel biological targets for detection and regulation. *Chem Soc Rev*. 2014;43(2):506–517. doi:10.1039/c3cs60312a
47. Ekin A, Karatas OF, Culha M, Ozen M. Designing a gold nanoparticle-based nanocarrier for microRNA transfection into the prostate and breast cancer cells. *J Gene Med*. 2014;16(11–12):331–335. doi:10.1002/jgm.2810
48. Choi KM, Choi SH, Jeon H, Kim IS, Ahn HJ. Chimeric capsid protein as a nanocarrier for siRNA delivery: stability and cellular uptake of encapsulated siRNA. *ACS nano*. 2011;5(11):8690–8699. doi:10.1021/nn202597c
49. Wu H, Lv WH, Zhu YY, Jia YY, Nie F. Ultrasound-mediated mesoporous silica nanoparticles loaded with PDLIM5 siRNA inhibit gefitinib resistance in NSCLC cells by attenuating EMT. *Eur Pharma Sci*. 2023;182:106372. doi:10.1016/j.ejps.2023.106372
50. Ma P, Li J, Gao Y, et al. Local and Systemic Delivery of the BimS Gene Nano-Complex for Efficient Oral Squamous Cell Carcinoma Therapy. *Int j Nanomed*. 2022;17:2925–2941. doi:10.2147/ijn.s357702
51. Cho WC. Exploiting the therapeutic potential of microRNAs in human cancer. *Expert Opin Ther Targets*. 2012;16(4):345–350. doi:10.1517/14728222.2012.663354
52. Khansa I, Schoenbrunner AR, Kraft CT, Janis JE. Silver in Wound Care-Friend or Foe?: a Comprehensive Review. *Plastic Reconst Surg Global Open*. 2019;7(8):e2390. doi:10.1097/gox.0000000000002390
53. Benyettou F, Rezgui R, Ravaux F, et al. Synthesis of silver nanoparticles for the dual delivery of doxorubicin and alendronate to cancer cells. *J Mater Chem B*. 2015;3(36):7237–7245. doi:10.1039/c5tb00994d
54. Zhu Y, Wen LM, Li R, Dong W, Jia SY, Qi MC. Recent advances of nano-drug delivery system in oral squamous cell carcinoma treatment. *Eur Rev Med Pharmacol Sci*. 2019;23(21):9445–9453. doi:10.26355/eurrev_201911_19438
55. Kumar P, Ning Y, Polverini PJ. Endothelial cells expressing Bcl-2 promotes tumor metastasis by enhancing tumor angiogenesis, blood vessel leakiness and tumor invasion. *Lab Investigat*. 2008;88(7):740–749. doi:10.1038/labinvest.2008.46
56. Duan Y, He Q, Yue K, et al. Hypoxia induced Bcl-2/Twist1 complex promotes tumor cell invasion in oral squamous cell carcinoma. *Oncotarget*. 2017;8(5):7729–7739. doi:10.18632/oncotarget.13890